Uncovering deformation processes from surface displacements

Salvatore Stramondo[1], Elisa Trasatti[1], Matteo Albano[1], Marco Moro[1], Marco Chini[2], Christian Bignami[1], Marco Polcari[1]

1 Istituto Nazionale di Geofisica e Vulcanologia, Via di Vigna Murata 605, 00143 Roma, Italy.

2 Luxembourg Institute of Science and Technology, 5, avenue des Hauts-Fourneaux, L-4362 Esch sur Alzette, Luxembourg.

Abstract

Today, satellite remote sensing has assumed a key role in Earth Sciences. In particular, Synthetic Aperture Radar (SAR) sensors and SAR Interferometry (InSAR) techniques are widely used for the study of dynamic processes occurring in our living planet. Over the past 3 decades, InSAR has been widely used for mapping topography and deformation at the Earth's surface. These maps are widely used in tectonics, seismology, geomorphology, and volcanology, in order to investigate the kinematics and mechanics of crustal faulting, the causes of postseismic and interseismic displacements, the dynamics of gravity driven slope failures, and the deformation associated with subsurface movement of water, hydrocarbons or magmatic fluids.

This review manuscript aims at providing the state of art of InSAR research activities and outcomes with a particular emphasis on applications involving new and most recent satellite missions. More in detail, this review paper focuses firstly on active tectonics, and in particular on the investigation of inter-seismic, pre-seismic, co-seismic, and post-seismic phases of the tectonic process over its temporal and spatial behavior. Then it focuses on discovering the volcanic activities by measuring and interpreting ground movements that reflect changes of pressure in shallow magma reservoirs or are caused by the occurrence of intrusive events. Indeed, the study of surface deformation is one of the key methods of inferring the geometrical and dynamical parameters characterizing buried magma bodies, especially if associated with the study of local seismicity. Volcanic uplift is a common precursor to eruptions, and the continuous monitoring that quantifies the spatial and temporal evolution of the deformation is an essential and powerful tool for near real time volcano hazard estimates.

1. Introduction

Nowadays, Earth observation by remote sensing sensors on board of spacecraft has assumed a key role in understanding the dynamic processes of our living planet. A huge number of techniques, methods and algorithms have been developed in the last decades, with the objective of deeply exploiting information encrypted in the satellite images.

Among these techniques, the role of remote sensing and in particular of the Synthetic Aperture Radar (SAR) sensors in detecting and measuring surface movements has been widened. Today, Earth Sciences have available innovative tools to generate a huge number of observations that better constrain ground deformations in order to improve the understanding of the physical processes beyond these natural phenomena.

The processes producing surface deformation cover a wide range of causes. Roughly, we can separate such deformations into two classes of causes: “natural” and “anthropogenic”. In a non-exhaustive list, natural deformation includes the seismic cycle and the deformation of volcanic edifices, while anthropogenic deformation includes land subsidence in urban areas due to urbanization and to overexploitation of water resources, the deformation related to fluid injection or withdrawal, the deformation of civil infrastructures (dams, buildings, nuclear power plants, etc.).

The accurate measurement of surface deformation is one of the most relevant parameters for studying the seismic cycle and, in particular, for modeling the mechanisms of tectonic stress accumulation and release. Displacements analyses, also at large scale through the synoptic capabilities of space sensors, unlock the opportunity to study inter-seismic, pre-seismic, co-seismic, and post-seismic phases of the tectonic process, over its temporal and spatial behavior.

Ground deformation is a phenomenon commonly observed in connection with volcanic activity. It is usually interpreted to reflect changes of pressure in shallow magma reservoirs or to be caused by the occurrence of intrusive events. The study of surface deformation is one of the key methods of inferring the geometrical and dynamical parameters characterizing buried magma bodies, especially if associated with the study of local seismicity. Volcanic uplift is a common precursor to eruptions, but, for some volcanoes, uplift of meters or more has not yet led to an eruption. The continuous monitoring that quantifies the spatial and temporal evolution of the deformation is therefore an essential and powerful tool for near real time volcano hazard estimates.

Satellite measurements are the best way to provide a fast, systematic and synoptic view of the Earth surface over large areas and long-term period, especially in remote areas where the setup of a monitoring network is not feasible. For such aims, Synthetic Aperture Radar (SAR) is the most relevant instrument today.

In this paper, the SAR technique is discussed by reviewing its development since the 1992, and then its powerful contribution showing several cases of study of seismic and volcanic surveillance and crisis.

2. InSAR: improvements on Science and Technology

2.1. SAR satellite missions: from past to present day

The history of civilian satellite SAR systems began with the 1978 NASA Seasat satellite, which was the first satellite equipped with a SAR sensor, operating at L band (24 cm of wavelength) of the electromagnetic spectrum. The mission was designed for remote sensing of the Earth's oceans to demonstrate the feasibility of global satellite monitoring of oceanographic phenomena and to help determining the requirements for an operational ocean remote sensing satellite system. Specific objectives were to collect data on sea-surface winds, sea-surface temperatures, wave heights, internal waves, atmospheric water, sea ice features, and ocean topography. In addition, it was also used to image the land in several areas but, unfortunately, the satellite lifetime was about three months. The first application of the SAR Interferometry (InSAR) technique exploited Seasat data to detect vertical motions over a few days caused by soil swelling of irrigated fields in the Imperial Valley, California, (Gabriel et al., 1989). The authors affirmed that InSAR "*can measure accurately extremely small changes in terrain over the large swaths associated with SAR imaging, especially since the sensor can work at night and through clouds or precipitations*".

In 1991 the European Space Agency (ESA) launched its ERS-1 satellite with a C-band (5.6 cm wavelength) SAR system, which was joined by ERS-2 a few years later (1995) (see Figure 1).

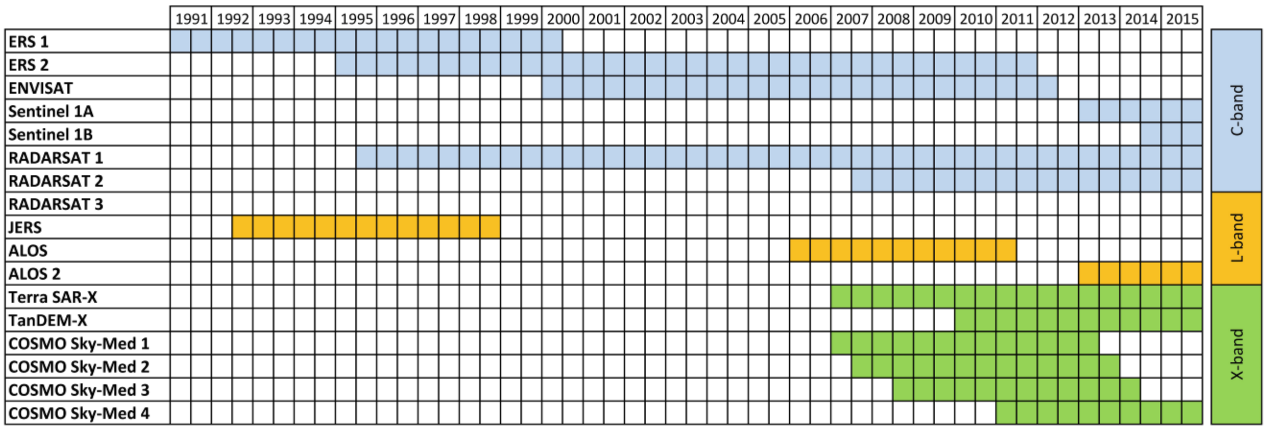

Figure 1: SAR satellite missions since 1991 (ERS-1) up to 2015 (Sentinel missions and others). The year 2010 is the best-covered year, because in late 2011 ERS2 and ALOS unfortunately ceased to operate, followed in 2012 by Envisat.

The applications using data from both SAR satellites spanned most of the Earth Sciences, and in 1993 the capability to apply the InSAR technique to ERS data was demonstrated for the case of the deformation due to the Mw 7.3 Landers earthquake in California (Massonnet et al., 1993) and ice motion in Antarctica (Goldstein et al., 1993). In parallel, the National Space Development Agency of Japan (NASDA, now JAXA - Japan Aerospace Exploration Agency) developed an L-band SAR sensor that was launched into orbit onboard the JERS-1 satellite, in 1992. The applications of JERS-1 were mostly focused on earthquakes and volcanic eruptions in Japan (Ozawa et al., 1997) or Asia in general (Tobita et al., 1998), while less used in Europe or America (Murakami, 1996) due to limited data coverage. In 1995, the Canadian Space Agency (CSA) launched RADARSAT-1, an advanced Earth observation satellite (http://www.asc-csa.gc.ca/eng/satellites/radarsat1/default.asp) to monitor environmental change and to support resource sustainability. This C-band SAR sensor had a number of different radar imaging modes, including wide-swath for large area imaging. RADARSAT-1 has been used in a wide range of applications: sea-ice monitoring - daily ice charts, extensive cartography, flood mapping and disaster monitoring in general, glacier monitoring, forest cover mapping, oil spill detection, assessment of the likelihood of mineral, oil and gas deposits, urban planning, crop production forecasts, coastal surveillance (erosion), and surface deformation detection (due to earthquake, volcanic or glacier movements). Many of these missions are now out of operation. JERS stopped collecting data in 1998, ERS-1 failed in 2000, ERS-2 was switched off in 2011, and communication with Radarsat-1 was lost in March of 2013.

In 2002, ESA launched Envisat, an advanced polar-orbiting Earth observation satellite, which provides measurements of the atmosphere, ocean, land, and ice. Among other instruments, Envisat operated an Advanced SAR (ASAR) system that was an improvement on the previous SAR systems. ASAR is a partially polarimetric system (capable of measuring different polarizations of the radar signal) with 7 imaging mode, each with a different incidence angle and different swath size, along with a wide-swath mode capable of producing 250-km-wide SAR images. An early target of Envisat displacement application was the 2003 Bam (Iran) earthquake (Fialko et al., 2005; Funning et al., 2005; Stramondo et al., 2005; Talebian et al., 2004), where the co-seismic deformation field was measured using acquisitions from both descending and ascending orbits.

From 2003 until 2010, the Envisat mission was the most important source of SAR data available for scientific research. At the end of October 2010, the satellite orbit was lowered and the orbital inclination was allowed to drift in the hope that the mission could be extended by as much as three years with the limited fuel remaining. In April of 2012, communication with Envisat was lost.

In January 2006, the JAXA launched the ALOS (Advanced Land Observing Satellite) mission. ALOS carried optical instruments – PRISM and AVNIR – and the Phased-Array L-band SAR (PALSAR) instrument. PALSAR is a flexible sensor, able to provide enhanced sensor performance, including full polarimetry, variable off-nadir viewing and wide-swath (ScanSAR) operations. Additionally, the spatial and temporal coverage of PALSAR was capable of achieving global coverage on a repetitive basis. ALOS operated until April of 2011, after imaging the displacement field of the impressive earthquake-tsunami in Tohoku-Oki (Japan), on March 11, 2011 (Feng et al., 2012). Starting in 2007, a new generation of high-resolution SAR systems was launched by several space agencies, capable to capture Earth images with pixel resolution down to 1 m size. The German Aerospace Agency (DLR) launched TerraSAR-X, an X-Band system able to operate in four modes (from High Resolution Spotlight, 1 m resolution, to ScanSAR, 18 m). TerraSAR-X data have been used to generate displacement maps of quite recent earthquakes, including the 2010 M7 Haiti (see the Group on Earth Observations, GEO - Geohazard Supersite and Natural Laboratories, GSNL, website http://www.earthobservations.org/gsnl_es_haiti.php) and the 2011 M9 Tohoku-Oki, Japan earthquake. In 2010, a second satellite joined the previous one in a close formation (orbiting only few hundred meters apart), thus starting the TanDEM-X mission aimed at generating a new, global, high-resolution SAR Digital Elevation Model (DEM).

The Italian Space Agency (ASI) launched its first high-resolution X-Band SAR satellite, COSMO-SkyMed-1, in 2007. COSMO-SkyMed's capabilities include very high resolution (up to 1 m), polarimetric modes and right-left lateral view options. In the following years up to November 2010, ASI completed a constellation of four satellites in order to improve the capabilities of the system, both in terms of revisiting time and unprecedented monitoring performance.

On the other hand, the CSA provided data continuity for RADARSAT-1 users with the RADARSAT-2 program. Along with additional imaging modes, RADARSAT-2 is designed with RADARSAT-1 compatible modes and follows the same orbit, repeat cycle, and ground track as well. New capabilities include the high-resolution (3 m) Ultra Fine mode, full polarimetric capabilities and right-left looking view. In particular, the full polarimetric (quad-pol) capabilities have found applications in wetlands and agricultural environments (Sang-Hoon, 2011).

According to the Japan's new space program, on May 2014 JAXA launched the second L-band satellite ALOS-2. The aim of the ALOS-2 mission is to give continuity to the SAR data utilization provided by ALOS for applications of cartography, regional observation, disaster monitoring, and environmental monitoring. ALOS-2 shows some advantages with respect to its predecessor. The observation frequency is strongly improved thanks to the capability of both right and left side looking of the satellite and the lower revisit time of 14 days (the revisit time of ALOS was 46 days). Moreover, apart from the Stripmap and the ScanSAR mode, a Spotlight acquisition mode is also implemented allowing acquiring data with a spatial resolution of about 1 m x 3 m.

On April 3, 2015, ESA launched the Sentinel-1A satellite from the European Spaceport in French Guiana. Sentinel-1A is the first of a constellation of two satellites (Sentinel-1A and Sentinel-1B) included in the Sentinel-1 SAR-dedicated mission. Each Sentinel-1 satellite is equipped with an advanced C-band polar-orbiting SAR sensor and it is designed to map the global landmasses once every 12 days, i.e., the revisit time has been improved of about a factor 3 with respect to the ERS and Envisat missions.

This satellite constellation is able of acquiring data in several modes varying the area coverage and the resolution thus being flexible to the needs required by the specific applications and the studied phenomena.

The more common acquisition mode is the Interferometric Wide swath (IW), a new type of ScanSAR called Terrain Observation with Progressive Scan (TOPS), which allows significantly extending the ground coverage with a 250 km swath at about 5 m range by 20 m azimuth spatial resolution.

Moreover, the system is able to acquire data also in Stripmap mode and in Extra Wide (EW) swath mode improving the pixel resolution (~5 m x 5 m) and the areal coverage (~400 km) respectively. Actually, these characteristics make Sentinel-1 a very powerful tool for the Earth's surface observation.

Sentinel-1A captured its first seismic event on 24 August 2014, when a Mw 6.0 earthquake occurred in Napa Valley, California, (Brocher et al., 2015). The eruption of the Fogo volcano (Cape Verde), started on November 23, 2014, and more recently, the co-seismic deformation produced by the 2015 Mw 7.8 Nepal earthquake were the first applications with Sentinel-1 data acquired in IW mode (Diao et al., 2015).

From the present and future satellite missions is emerging that we are moving towards the era of SAR constellations, equipped with different sensors, different characteristics and capabilities, that will allow to study many types of geophysical phenomena. Actually, deformation processes acting with different velocities, mechanisms and directions, can require specific strategies of acquisitions and revisit times, and also SAR wavelengths can impact on the capability to measure such phenomena. In Figure 2 there is a summary of the crustal deformation classified by rate and duration and the capabilities, in terms of revisiting time and displacement detection accuracy, of the new and previous SAR missions. It illustrates how the large availability of data is now unlocking the better estimation and comprehension of ground deformation at different spatial and temporal scales.

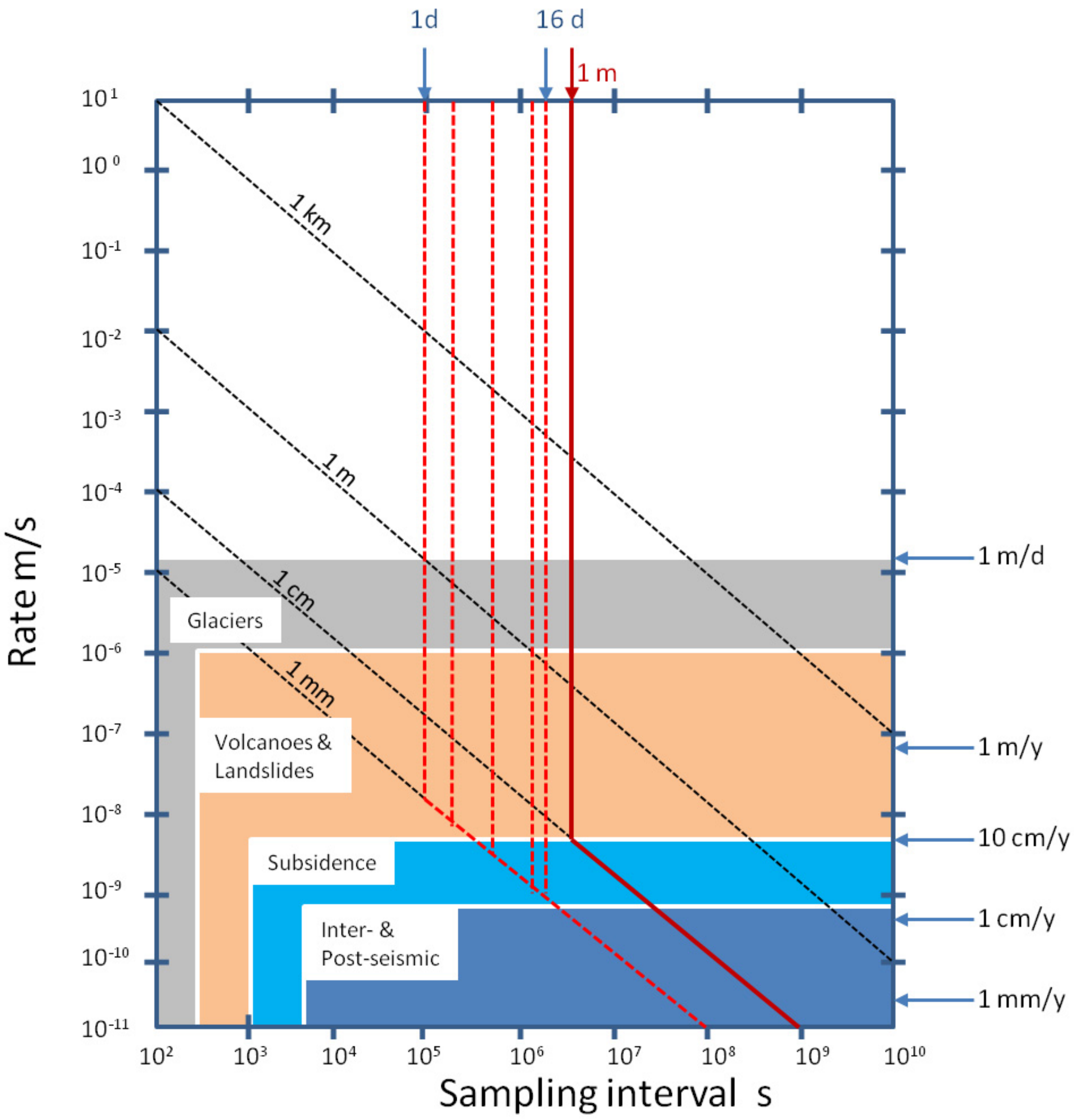

Figure 2:Crustal deformation classified by rate and duration, adapted from Plate 16 of Massonnet and Feigl (Massonnet and Feigl, 1998). The product of such two quantities provides the total amount of deformation (black dashed lines) in a given time interval. The solid red line shows the case of a pass every 35 days and 1 cm precision. The figure considers also the most recent cases, including few days temporal interval between two passes up to 11-16 days (TerraSAR-X and COSMO-SkyMed, if repeat pass is computed over one satellite).

2.2. Basic concepts of InSAR technology

InSAR is a data processing technique aimed at measuring any change of phase component of two or more SAR images properly acquired over the same orbit. InSAR has demonstrated to be a reliable tool for measuring Earth surface movements, and for providing reliable inputs to constrain the sources of the deformation. InSAR has been successfully used to investigate the surface expression of natural disasters and anthropogenic effects, including earthquakes, volcanic eruptions (Figure 3), landslides, slope instabilities, and land subsidence.

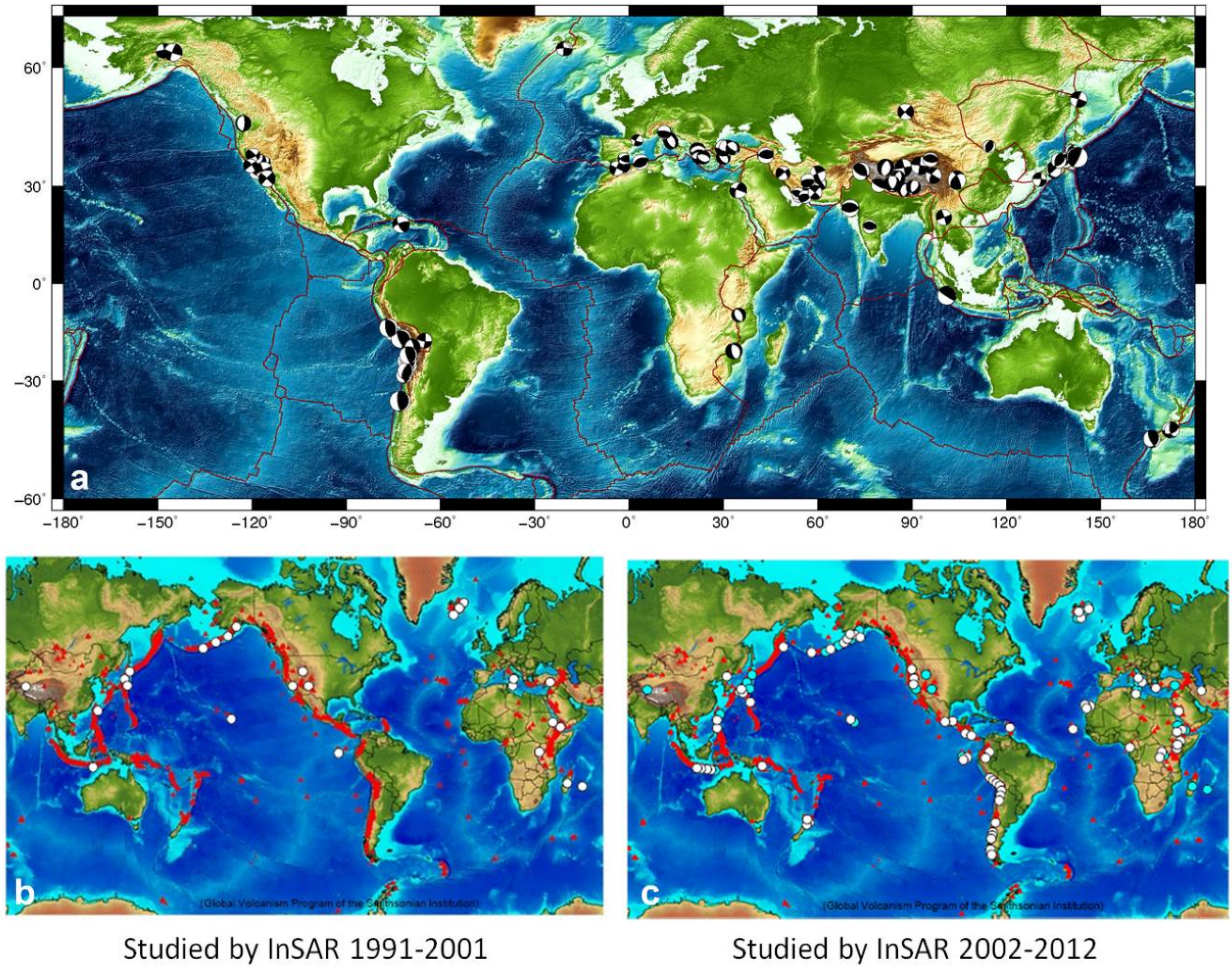

Figure 3: (a) Earthquakes studied in 1992-2012 (Figure updated from Wright et al., 2013) based on the use of InSAR; (lower) Volcanic studies (white dots) in 1991-2001 (b) and in 2002-2012 (c) (white dots; cyan dots are those in 1991-2001) (from http://globalvolcanomodel.org/gvm-task-forces/volcano-deformation-database/) using InSAR.

The result from InSAR is called *interferogram*. The interferogram is a map of per pixel phase difference between two SAR images, captured with the same mode, with a very similar geometry, and on the same nominal orbit. Actually, the SAR images have to be on interferometric configuration in order to be a suitable interferometric pair. The phase differences of the interferogram pixels, i.e., the interferometric phase, can be schematically split into five terms: the flat Earth component, the topographic phase, the displacement phase, the atmospheric term, and the error phase (Bürgmann et al., 2000). Going deep in explaining such terms is outside the scope of this work, however the displacement phase stands for the phase contribution due to the change of satellite to target distance caused by the surface modifications. Some of the remaining phase terms can be estimated by exploiting information on orbital flight (flat Earth phase), on elevation by means of an external DEM (topographic phase), some others are source of uncertainty (the atmospheric and error phases). It is worth noting that if referred to displacements, the technique is known as Differential InSAR (DInSAR), which measures the projection of the displacement vectors along the satellite Line Of Sight (LOS), i.e., the sensor-to-target straight line. Therefore, the detected movement is the projection of the 3D components into the LOS.

2.3. Multi-temporal InSAR and Time series

The geophysical scientific community has extended the focus from the investigation of large surface displacements of natural disasters toward the monitoring of the temporal and spatial evolution of the Earth's surface. This produced a need to develop innovative SAR processing techniques whose main emphasis is the comprehensive exploitation of the available datasets in order to cover the full time span since the first acquisition. The use of tens or hundreds of images allows for dense temporal sampling of the investigated period using available data from each satellite revisit (Hooper et al., 2011). These new SAR data processing techniques are generically named Multi-temporal InSAR or Advanced InSAR (A-InSAR). A variety of A-InSAR algorithms and procedures have been developed by a number of research teams, since 2000 (Agram et al., 2013; Berardino et al., 2002; Crosetto et al., 2005; Ferretti et al., 2000; Hooper et al., 2004; Mora et al., 2003; Schmidt, 2003; Shirzaei, 2012; Usai, 2003; Werner et al., 2003); (Biggs et al., 2007a). Despite the different approaches, they all share the following aspects:

1) A-InSAR deals with the use of a large number of SAR data, namely a stack of images with the same acquisition mode and geometry;
2) A-InSAR is focused on the measurement of slow surface movements (centimeters and/or millimeters per year);
3) A-InSAR can be applied to follow the time-varying evolution of a surface deformation process.

These capabilities can be achieved thanks to the multiple estimates of each term of the interferometric phase. Indeed, using large SAR datasets allows increasing the capability to properly model the displacement phase contribution and to follow the temporal and spatial evolution of the phenomenon, and at the same time reducing the uncertainties by a better knowledge of the other interferometric phase terms. For example, the A-InSAR can improve the estimate of the topographic component of the phase, allowing an improved displacement modelling. In addition, the A-InSAR techniques can estimate the atmospheric phase contribution, also known as atmospheric phase screen (APS), which is one the most disturbing information for interferometry. In contrast to standard DInSAR processing approaches, A-InSAR techniques usually compute the phase differences of SAR data for those pixels of the images that are effectively stable, from the electromagnetic point of view, through time, which are defined as coherent pixels. These methods can be considered as point-wise approaches.

A-InSAR techniques can be classified according to the methodology involved. In general, we can distinguish between two main approaches developed in the early 2000s: the PS-Permanent Scatterer method (Ferretti et al., 2000) and the SBAS-Small Baseline Subsets method (Berardino et al., 2002); (Lanari et al., 2004). PS is a single-master technique working with full resolution data and focusing on identifying pixels based on the stability of the SAR coherence or amplitude. On the other hand, SBAS can be applied to averaged data and is based on a multi-baseline approach aiming at reducing the decorrelation effects. Some slight modifications of these two approaches led to other A-InSAR techniques such as CPT-Coherent Point Targets (Mora et al., 2003), WabInSAR (Shirzaei, 2012), MInTS (Hetland et al., 2012), pi-rate (Biggs et al., 2007b), StaMPS (Hooper et al., 2004), IPTA-Interferometric Point Target Analysis (Werner C. et al., 2003) and SPN-Stable Point Network (Crosetto et al., 2005).

We note that both approaches are effective as it is demonstrated by several published results, with advantages and disadvantages depending on the nature of the data or target application (Hooper, 2008). Generally, the techniques listed in the first group seem to be more suitable for regions of the Earth surface with higher coherence. Indeed, as the coherence is computed on a spatial window whenever a single coherent pixel is within a low coherence region it can be missed because the "average" over the search window is below the threshold. In contrast, the second group of techniques generally deals with full-resolution applications. This implies that although a single persistent pixel is close to other incoherent pixels, it can provide precise information about its own history. Recently, methods have combined the two approaches to extract information on both point-like scatterers and distributed but still stable areas (Ferretti et al., 2011; Hooper, 2008).

When considering the so-called Persistent or Permanent Scatterer we need deep a stack of observations to be able for evaluating the stability of the targets. Long term, high-coherence interferograms are rare, because many pixels will undergo some changes (due to vegetation growth or local strong ground motion) that lead to random changes in the returned phase, hence a loss of phase stability. Nonetheless, many individual pixels will remain unchanged even for decades especially in the urban scenarios. Typically, these target points correspond to man-made, natural or artificial reflectors such as buildings, roads, outcropping rocks, etc. To have reliable detection, and for a good estimate of motion and actual height for each pixel, the use of at least 15 – 20 images is required. Keeping the orbital paths of the satellite close each other (the so-called narrow orbital tube), the impact of topography becomes lower, and the use of lower quality DEMs can be acceptable.

If relatively narrow orbital tubes are maintained, the use of SBAS-type methods (Berardino et al., 2002; Lanari et al., 2004) for long-term motion estimation becomes feasible. In this case, the effect of topographically induced bias is easily compensated, and only the atmospheric phase component has to be removed.

The two methodologies, SBAS and PS-InSAR yield similar results when the baselines have small dispersion: the PS methodology is computationally more expensive, but has the advantage of a denser set of stable points and a better estimate of the atmospheric contribution. In the case where the persistent scatterers are very dense, as in desert or urban areas, the two methodologies yield very similar results.

In the new version of the PS algorithm, SqueeSAR (Ferretti et al., 2011), the temporal smoothing can be obtained by considering the covariance matrix of the same spatial window along all the takes.

3. The knowledge of tectonic processes

InSAR has proven to be a particularly powerful technique for earthquake geodesy – particularly in areas where no ground-based geodetic observations are available. Recent compilations have found more than 90 earthquakes for which InSAR has been used to derive focal mechanisms from co-seismic deformation observations, 28 InSAR studies of interseismic strain accumulation, and 23 earthquakes in which InSAR had contributed to the monitoring of post-seismic deformation (Weston et al., 2012; Weston et al., 2011) (Wright et al., 2013). The observed surface deformation from earthquakes (coseismic deformation) is mainly caused by the amount of fault dislocation and the fault geometry. For large ($Mw \geq 6$) earthquakes, elastic dislocation modeling allows for the determination of finite slip distributions of the rupture through inversion for the geometry and distributed slip on a discretized grid of dislocations. The investigation of transient post-seismic deformation during the days to years after an earthquake can be performed using a large number of SAR images and A-InSAR techniques. The study of interseismic deformation allows for characterization of the long-term elastic strain accumulation along a fault preceding an eventual earthquake and detection of transient fault slip events.

3.1. Coseismic studies

Seismic source parameters are being traditionally determined from seismology. When the results are compared systematically, seismologic and geodetic models broadly agree. However, InSAR data enable the fault location and certain geometric parameters to be determined more accurately for shallow earthquakes, and commonly do not suffer from the nodal plane ambiguity of point source seismic inversions (e.g. (Weston et al., 2012)).

Coseismic surface deformation measurements from InSAR can be inverted to retrieve geometrical parameters of the seismic source and the distribution of slip on the fault plane. The Landers earthquake (1992) was the first ever case study where interferometric analysis of a pair of ERS-1 acquisitions produced detailed images of the coseismic displacement field (Massonnet et al., 1993; (Zebker and Rosen, 1994). The data revealed the complex deformation surrounding a series of discontinuous strike-slip rupture segments in the Mojave Desert that stretched over about 70-km length. The maximum relative change in LOS produced by the earthquake was about 1 m across the fault, caused by around 6 m of slip on the fault.

Although InSAR is most useful for earthquakes larger than Mw ~ 6, it has been used in the case of very shallow small-magnitude events. This is the case of an earthquake sequence occurred in 2001 around the urban area of Spokane (Washington, USA), where the use of InSAR has allowed to detect a shallow previously unknown thrust fault, leading to assess the hazard potential of such seismic source (Wicks, 2013). Moreover in Western Australia (Dawson, 2008) a significant surface deformation (about 25 cm) resulted from a Mw 4.7 shallow (less than 1 km deep) event.

InSAR has proved to be of particular value in the characterization of a number of moderate earthquakes. In 2009, the city of L'Aquila (Central Italy) was hit by a seismic sequence whose main event (Mw 6.3) occurred very close to the historical center. The 2009 L'Aquila earthquake is the first ever case study where X-, C- and L-band SAR data were available for the same earthquake (Figure 4) (Stramondo et al., 2011b). Coseismic interferograms from COSMO-SkyMed, Envisat and ALOS PALSAR data were acquired, covering different time spans and with different temporal and spatial baselines. The large number of SAR images spanning the mainshock recorded the surface displacement pattern in great detail. Thanks to InSAR it was possible determine the surface trace of the fault responsible for the mainshock, the Paganica fault (Atzori et al., 2009). In addition, COSMO-SkyMed data in Stripmap mode (3 m resolution) and a high resolution (5 m) DEM detected local gravitational slope failures reactivated by the mainshock (Moro et al., 2011). The high spatial resolution and short wavelength of the COSMO-SkyMed X-band SAR allowed for an accurate assessment of these small deformation features (4–5 cm) triggered by the L'Aquila earthquake.

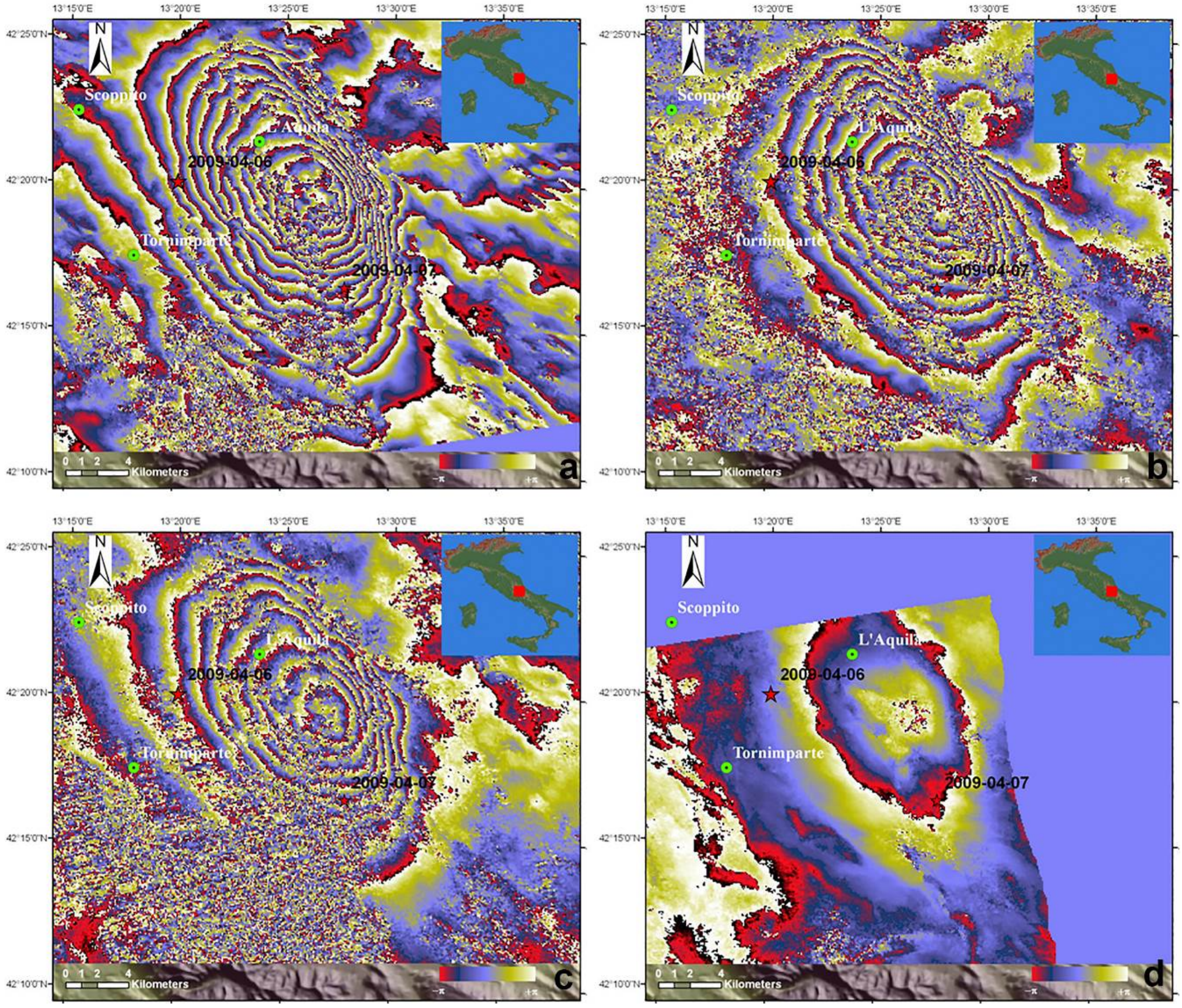

Figure 4: X-, C- and L-band wrapped interferograms of the L'Aquila 2009 earthquake (The study area is the red square in the top right inset). From upper left clockwise: (a) COSMO-SkyMed; (b) Envisat descending; (c) ALOS PALSAR; (d) Envisat ascending. Figure from (Stramondo et al., 2011a).

The destruction potential of moderate, shallow earthquakes has been also demonstrated in 2011 in New Zealand (Stramondo et al., 2011c). It is the case of the towns of Darfield (Canterbury) and Christchurch in New Zealand that were hit by two earthquakes within a time span of a few months. The Mw 7.1 Darfield earthquake took place on September 3, 2010 followed by a sequence of large aftershocks to the east including the Mw 6.3 Christchurch earthquake on February 21, 2011 (Figure 5) (Beavan et al., 2011; Beavan et al., 2012; Beavan et al., 2010). The Darfield (Canterbury) earthquake occurred along a previously unrecognized east-west fault line, the strike-slip Greendale fault (Beavan et al., 2010; Stramondo et al., 2011c). The Darfield earthquake ruptured a complex set of strike-slip and secondary reverse faults (Figure 6) (Barnhart W. D., 2011); (Elliott et al., 2012). Such details of the fault geometry would be extremely difficult to resolve with ground-based geodetic observations, even in regions with dense networks of continuously operating GNSS stations. The hypocenter of the Christchurch event was approximately 6 km south-east of Christchurch's city center, at a depth of 5–6 km, rupturing a blind ENE-striking oblique-thrust fault at the easternmost limit of the Darfield aftershocks.

In order to understand the role of the first earthquake in promoting the rupture of the second event, the Coulomb Failure Function (CFF) has been estimated (Figure 6). The CFF is obtained by computing the stress tensor corresponding to the elastic dislocation induced by the Canterbury earthquake, projecting it onto the rupture plane of the Christchurch earthquake. The stress perturbation promoted the second earthquake, even though without a clear knowledge of the starting stress level of the second fault it cannot be stated whether this latter was (or not) already likely to occur (Stramondo et al., 2011c). In both earthquakes, ALOS PALSAR pairs have been used to measure the coseismic movements, and additional InSAR from TerraSAR-X and COSMO-SkyMed improved the February 2011 Christchurch earthquake measurements.

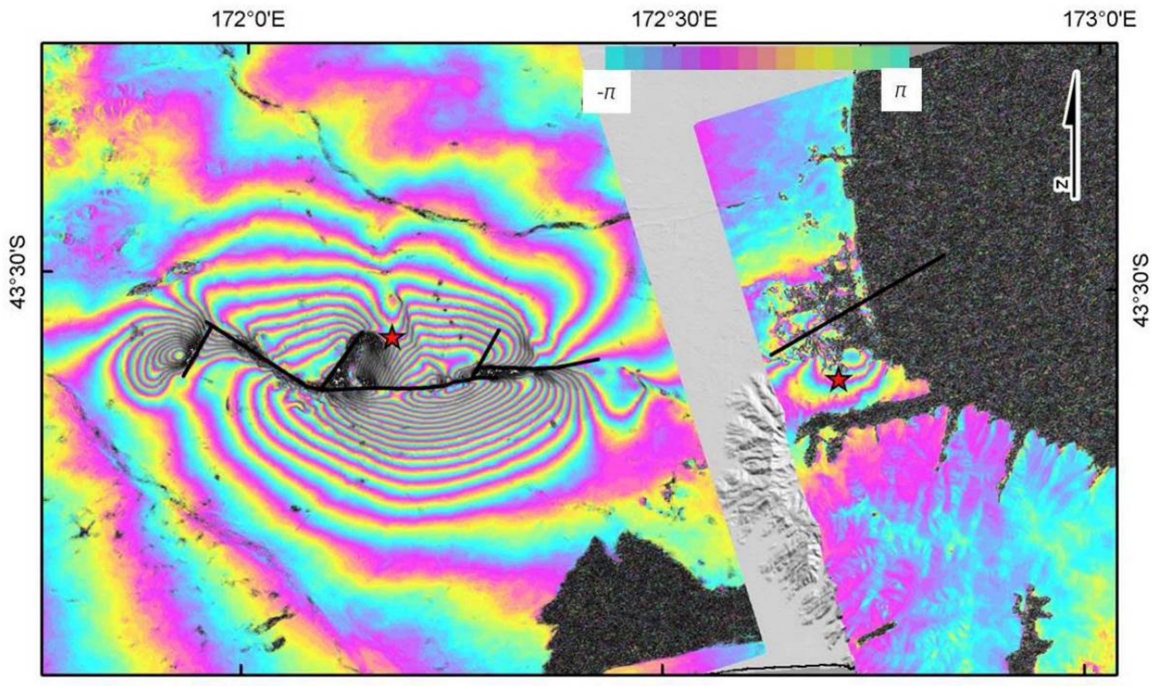

Figure 5: ALOS PALSAR interferograms of the September 3, 2010, Darfield (left) and February 21, 2011, Christchurch earthquakes. Each color cycle corresponds to a phase change of 2π that corresponds for PALSAR to 115 mm. Red stars indicate the epicenters of the September 3 (left) and February 21 (right) earthquakes. Black lines show the faults traces. From (Stramondo et al., 2011c).

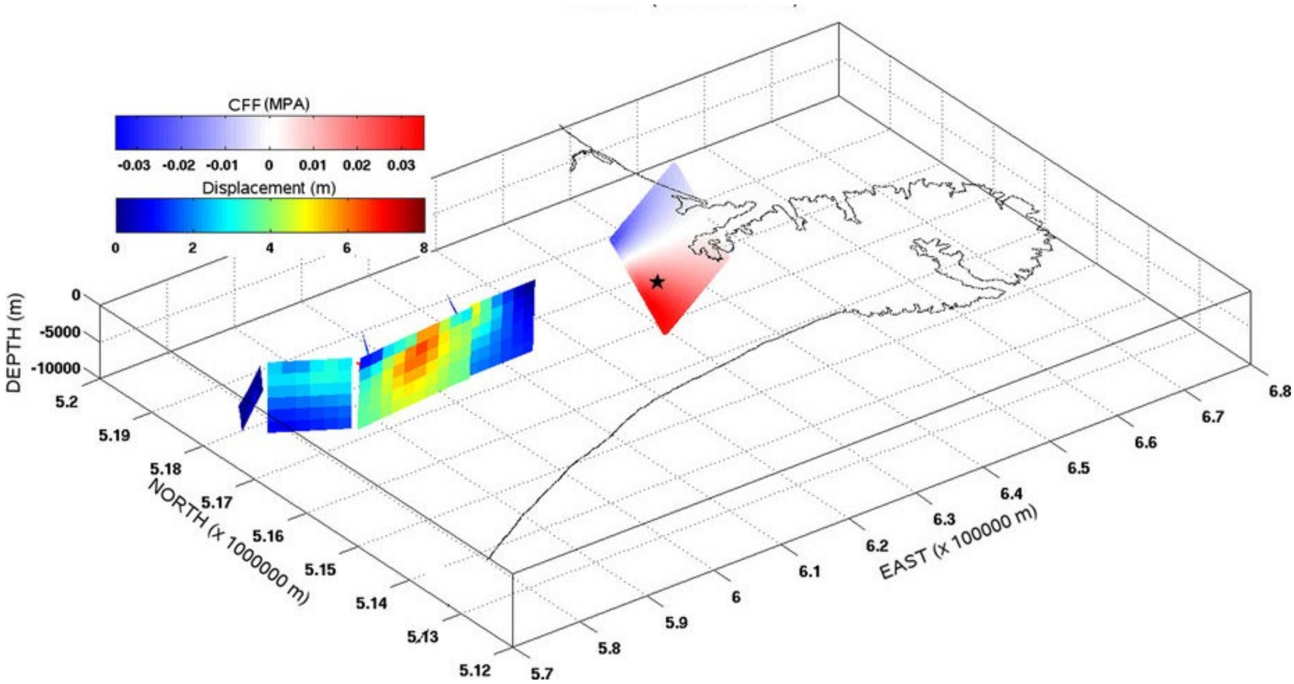

Figure 6: 3-D view of the fault planes adopted for the Darfield 2010 and for the Christchurch 2011 earthquakes. Fault slip over the Darfield patches is mainly concentrated in the central portion. Coulomb Failure Function (CFF), computed over the Christchurch fault plane, shows high values around the hypocenter of 2011 earthquake (Stramondo et al., 2011c).

Another example of a very complex fault rupture is the destructive M_w 7.9 Wenchuan earthquake that struck the western Sichuan province (China) in May 2008 along the topographic escarpment between the Tibetan Plateau and the Sichuan basin. The coseismic rupture involved a primary thrust-faulting component with an increasing contribution of strike-slip movement along the northern portions of the rupture, resulting in both vertical and horizontal displacements in excess of 6 m. Many groups around the world performed independent analyses of the InSAR and pixel offset data for the Wenchuan earthquake (Chini et al., 2010; De Michele et al., 2010; Feng et al., 2010; Fielding et al., 2013; Furuya et al., 2010; Hao et al., 2009; Shen et al., 2009; Tomokazu Kobayashi, 2009; Tong et al., 2010). The coseismic deformation field was measured with ALOS PALSAR InSAR using 25 frames along 6 tracks in image mode, along with limited Envisat data (Shen et al., 2009), and also with interferograms from the ALOS PALSAR (Tong et al., 2010) and Envisat, that acquired data in ScanSAR or wide-swath mode (Fielding et al., 2013). The results from all groups were broadly consistent, showing strike-slip motion along the 145-km-long Yingxiu–Beichuan fault and predominantly thrust faulting along the sub-parallel, 105-km-long Beichuan–Qingchuan fault (Chini et al., 2010).

The disastrous Tohoku-Oki megathrust earthquake (Mw 9.0) occurred on 11 March, 2011 near the NE coast of Honshu island (Japan). The initial seismological analysis indicated that a surface of about 300 km x 150 km over the fault moved upwards of 30-40 m (Sugawara et al., 2012). Soon after the earthquake, most of the Space Agencies made their satellite data of the epicentral region available free of charge via the GEO - GSNL initiative (http://www.earthobservations.org/gsnl_es_sendai.php). JAXA, ESA, DLR (German Space Agency), NASA (National Aeronautics and Space Administration), ASI, and CNES (French Space Agency) provided a large number of SAR and optical images even though each Agency has different data distribution. The coseismic interferograms from the 2011 Tohoku-Oki earthquake show a great amount of surface deformation over all of northeastern Japan with a maximum line-of-sight displacement of up to 3.7 m from the ascending PALSAR tracks and 2.4 m from the descending ASAR tracks, respectively (Feng et al., 2012). However, because the slip on the subduction interface was at a large distance from the onshore geodetic observations, the InSAR data added little new information in Japan, where ground-based GNSS observations are dense (Feng and Jónsson, 2012). Nevertheless, the localized deformation due to Mw 6 - Mw 7 aftershocks could be measured (Fukushima et al., 2013; He et al., 2013).

In countries where dense GPS are not available, InSAR data alone can be used to invert for the slip distribution on the subduction interface (Feng and Jónsson, 2012; Pritchard, 2006) The Earth Sciences community is also investigating the active role of earthquakes in causing major deformation over volcanic edifices. The Maule earthquake (2010, Chile) triggered subsidence between about 5 cm to 15 cm at five volcanoes (Figure 7) along a North-South line that is parallel to the modeled offshore displacement (i.e., coseismic slip) caused by the earthquake (Pritchard et al., 2013). The subsidence is attributed primarily to the release of hydrothermal fluids beneath the surface. As no significant thermal activity has been detected before and after the earthquake (ASTER - Advanced Spaceborne Thermal Emission and Reflection Radiometer and MODIS - Moderate Resolution Imaging Spectrometer data have been used), fluid migration has been identified as the cause for measured subsidence. Indeed, similar observations at volcanic regions in Japan after the 9.0 Tohoku earthquake suggest that magmatic systems parallel to major subduction zones can typically be squeezed by large earthquakes causing fluid migration.

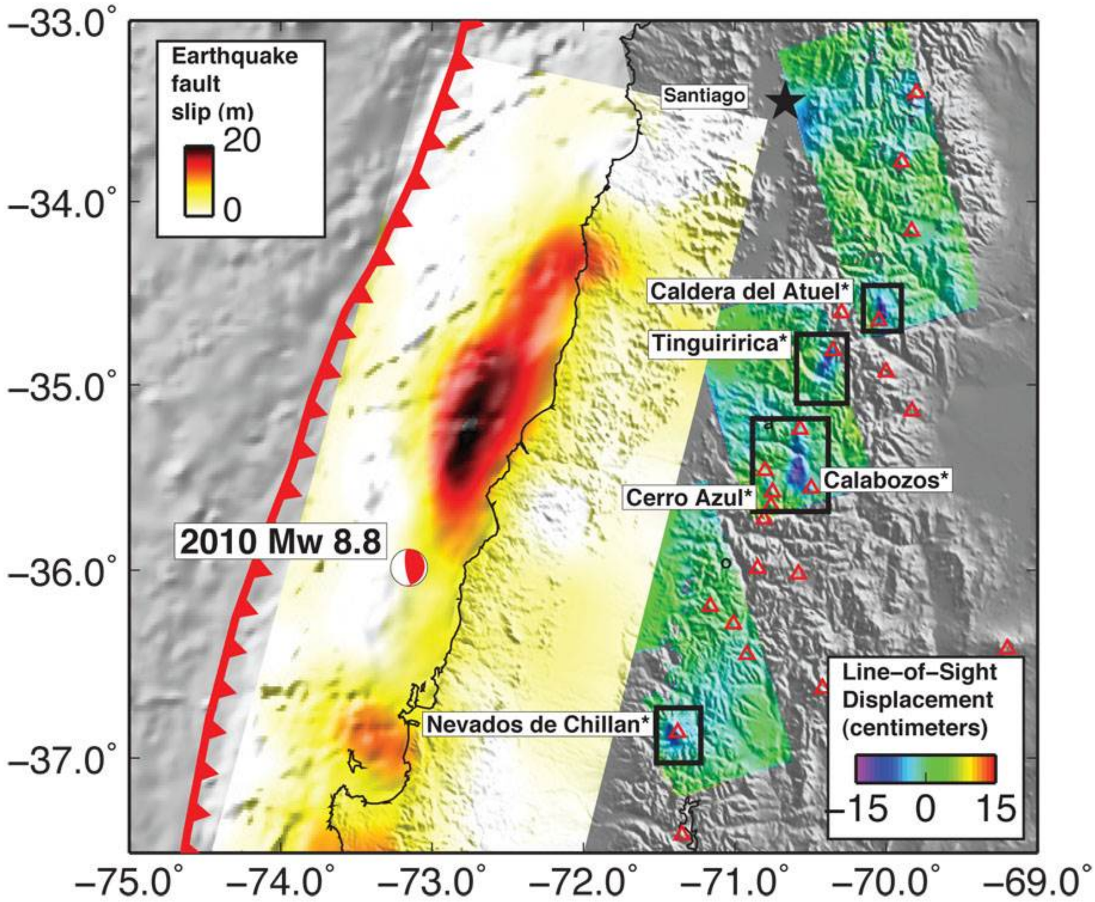

Figure 7: Map of southern Chile showing the location of earthquake fault slip from the Maule, Chile earthquake in 2010 (Mw 8.8) and images from satellite radar of ground subsidence (up to 15 cm) at 5 volcanoes triggered. From (Pritchard et al., 2013).

3.2. Earthquake secondary effects: soil liquefaction and Deep-seated gravitational slope deformations

3.2.1. A SAR perspective of liquefaction induced by seismic event

A secondary effect that can be measured by InSAR is the liquefaction phenomena caused by earthquakes. Such manifestations consist on sand boils, water leaks from cracks on the ground, and horizontal and vertical displacements, whose magnitude is strictly related to the geometrical and geotechnical features of the affected area. Ground deformations may have dramatic consequences such as instabilities of buildings, slopes and earth retaining structures.

An example of liquefaction-induced instabilities has been observed after the 2012 Emilia (Italy) earthquake (Chini et al., 2015). The earthquake shaking produced an excess of pore water pressure and the consequent liquefaction of deeper sandy soil strata. The related effects where numerous sand boils and water leaks from cracks suddenly opened at the ground surface, together with a diffused pattern of ground displacements. Because of these complex mechanisms, localized subsidence was observed, sometimes accompanied by ponding, which caused damages on many buildings, roads, fenced walls, and lifelines. For this particular event, the capability of InSAR have exploited to detect soil liquefactions occurrence and estimate their surface displacements.

The backscattering and its features (e.g., complex coherence and intensity correlation) from COSMO-SkyMed X-band SAR images were used for the detection of liquefaction insurgence, especially in urban areas. These SAR features allowed the identification of zones affected by differential compaction occurred in urban areas, probably associated to a volumetric deformation of the ground induced by liquefaction of saturated sandy deposits. For this particular event, the liquefaction did not cause big collapses to the buildings, the reason why the co-seismic intensity correlation remains quite stable (Figure 8). Indeed, the reduction of intensity correlation can be observed particularly when the backscattering characteristics of the surface changed drastically, which is the case of damages to buildings (Chini et al., 2008; Chini et al., 2009; Chini et al., 2012; Stramondo et al., 2006) that in the Emilia earthquake occurred in a limited amount. It is worth mentioning that, although these two parameters can measure how much the surface has changed between the two SAR acquisitions, they carry different information about the changes in the scene. The complex coherence is mostly influenced by the phase difference between radar returns, a distinctive parameter measured by a coherent sensor such as SAR, and it is particularly related to the spatial arrangement of the scatterers within the pixel and thus to their possible displacements. Conversely, the intensity correlation is more related to change in the magnitude of the radar return. This kind of behaviour was also observed in the case of the 2011 Tohoku (Japan) earthquake, where the seismic magnitude was very high and the SAR sensor was working at longer wavelength (C-band) (Chini et al., 2013). The analysis of the computed maps of coherence and intensity correlation showed clear features associated to the ground subsidence phenomena, resulting from the strong shaking and the pervasive liquefaction that affected the area.

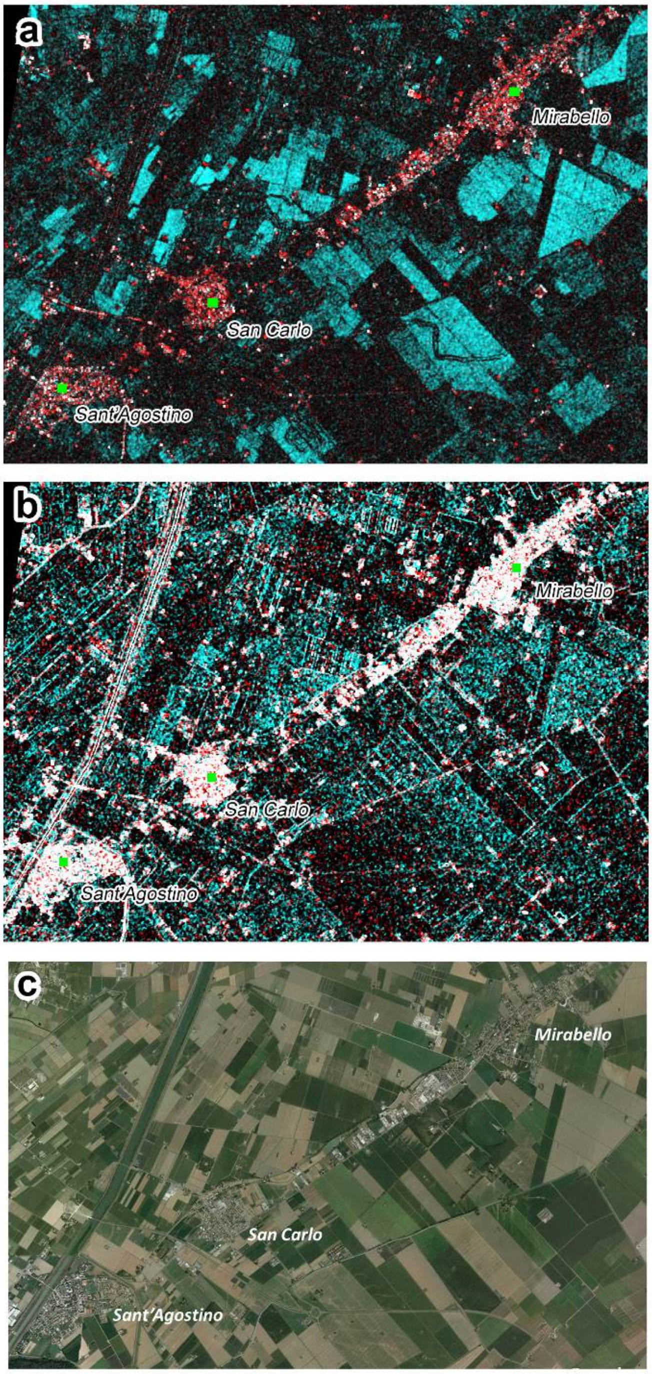

Figure 8: Details of the villages where liquefaction occurred. (a) RGB colour composite of two SAR coherence images [R: preseismic (April 1–May 19, 2012); G = B: coseismic (May 19–May 23, 2012)]. (b) RGB colour composite of two SAR intensity correlation images [R: preseismic (April 1–May 19, 2012); G = B: coseismic (May 19–May 23, 2012)]. (c) Optical image of the same area from Google Earth (Chini et al., 2015).

One of the most relevant results is the capability of SAR data to detect small settled areas where no surface effects, such as sand boils or cracks, were observed. In fact, regions with localized deformations, reaching a maximum subsidence value of about 6 cm, have been identified by DInSAR measurements (Figure 9). In these areas, neither surface cracks, nor sand ejections were detected by ground surveys. The measured displacements were attributed to the compaction induced by the liquefaction of deep sandy layers. To quantitatively confirm such a hypothesis, a series of liquefaction assessment analyses, together with the calculation of liquefaction induced settlements, were conducted in the studied area. The performed analyses have repetitively shown that the observed DInSAR settlements can be attributed to the liquefaction-induced compaction of a sandy soil layer at about 10 m depth.

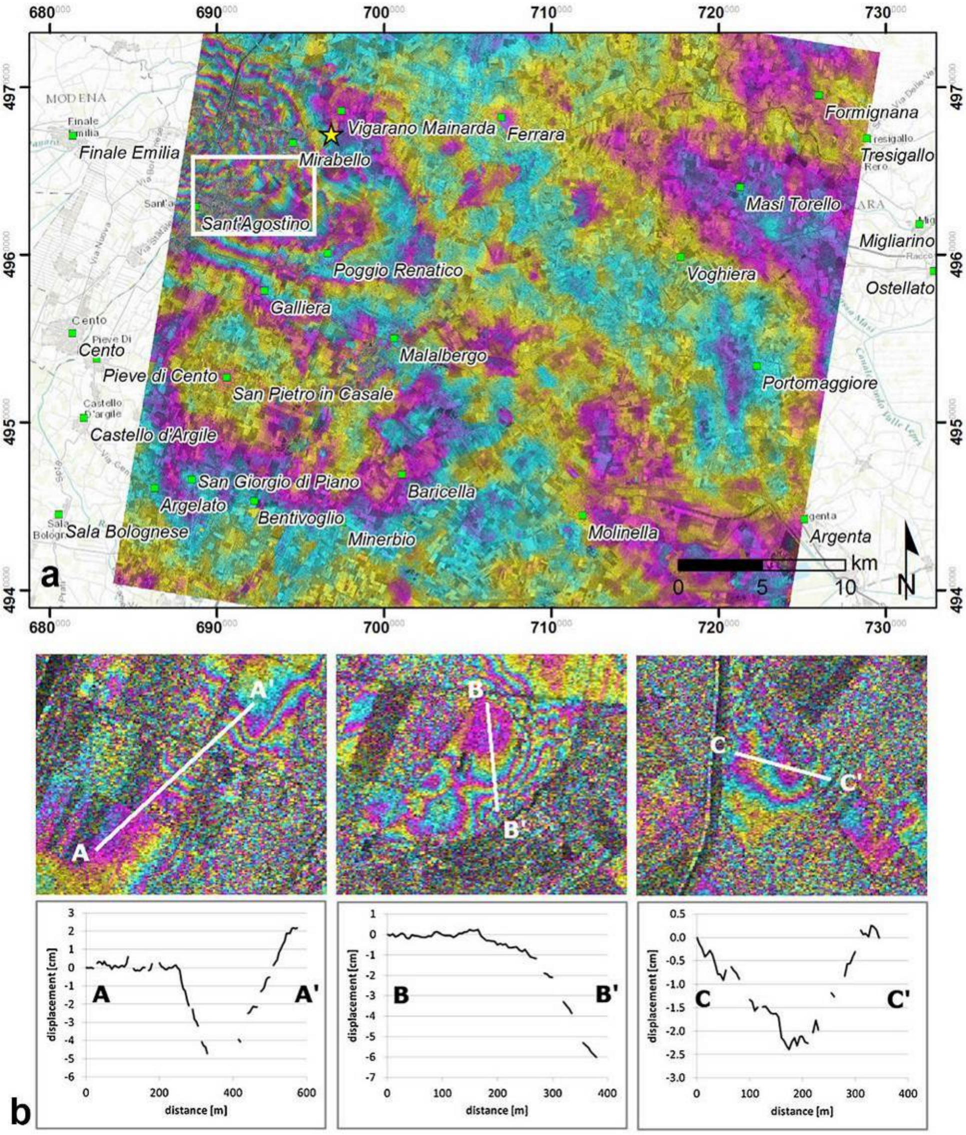

Figure 9: (a) COSMO-SkyMed interferogram of the epicentral area. (b) Detail of the measured deformation for three small areas identified in the area inside the white rectangle in panel (a). Upper panels report the three zoomed portions of the interferogram, lower panels show the observed subsidence along the profiles displayed in the upper panels (Chini et al., 2015).

3.2.2. Deep-seated gravitational slope deformations

Deep-seated gravitational slope deformations (DGSD) can be considered as gravitational movements involving large rock volumes in high-relief mountain areas. They typically affect the whole hillslope for thickness larger than several tens of meters and lengths of some kilometers (Moro et al., 2007). Moreover, it is common knowledge that the shaking caused by large earthquakes can induce gravitational collapses. In favorable conditions, the dynamic stress caused by the seismic excitation of a rock or soil mass adds to the local (static) stress level and may trigger an acceleration causing mass sliding and collapse (e.g., (Keefer, 1984)). In case of large earthquakes (Mw > 6.5) this process can lead to the formation of several collapses of rock/soil masses, which can significantly increase the damage level in densely developed areas. The landslide collapse is only the most evident observational end member of discontinuous ground deformation, while partially continuous (i.e., not involving collapse) gravitational deformations can be visually appreciated only when they involve changes of the ground surface shape of the order of meters or more. Their detection is extremely difficult for changes smaller than 10^{-1} m on single slopes, unless the area is being monitored by dense geodetic networks. For this reason, in areas hit by large earthquakes we may miss the evidence of triggered deformation, which could subsequently evolve toward catastrophic collapse. Only recently the DInSAR technique has expanded its capacity to detect small ground deformations at the local scale, such as for the DGSD (Moro et al., 2011). This is thanks to X-band SAR satellite sensors that now achieve a considerable improvement in spatial resolution and displacement measurement accuracy, whilst in the past its use was limited by spatial resolution and accuracy issues (Moro et al., 2007).

A worth mentioning example is the 2009 L'Aquila (Italy) earthquake, where COSMO-SkyMed X-band SAR was employed to identify local patterns of spatially continuous ground deformation which would have otherwise been overlooked. Indeed, high spatial resolution and good accuracy of the displacement estimates is mandatory to use SAR in geological analysis. Moro et al. show how the DInSAR technique, along with the high spatial resolution and the short wavelength of the COSMO-SkyMed images allowed an accurate assessment of small (4–5 cm), nearly instantaneous deformations triggered by the moderate magnitude L'Aquila earthquake (Figure 10). In Moro et al. (Moro et al., 2011), the geological analysis shows that localized measured deformations, within the larger co-seismic deformation field, occurred over previously unknown large gravitational mass movements. The authors highlighted that the ground deformation patterns described cannot be mapped with similar detail by any other geodetic method nor geological investigation.

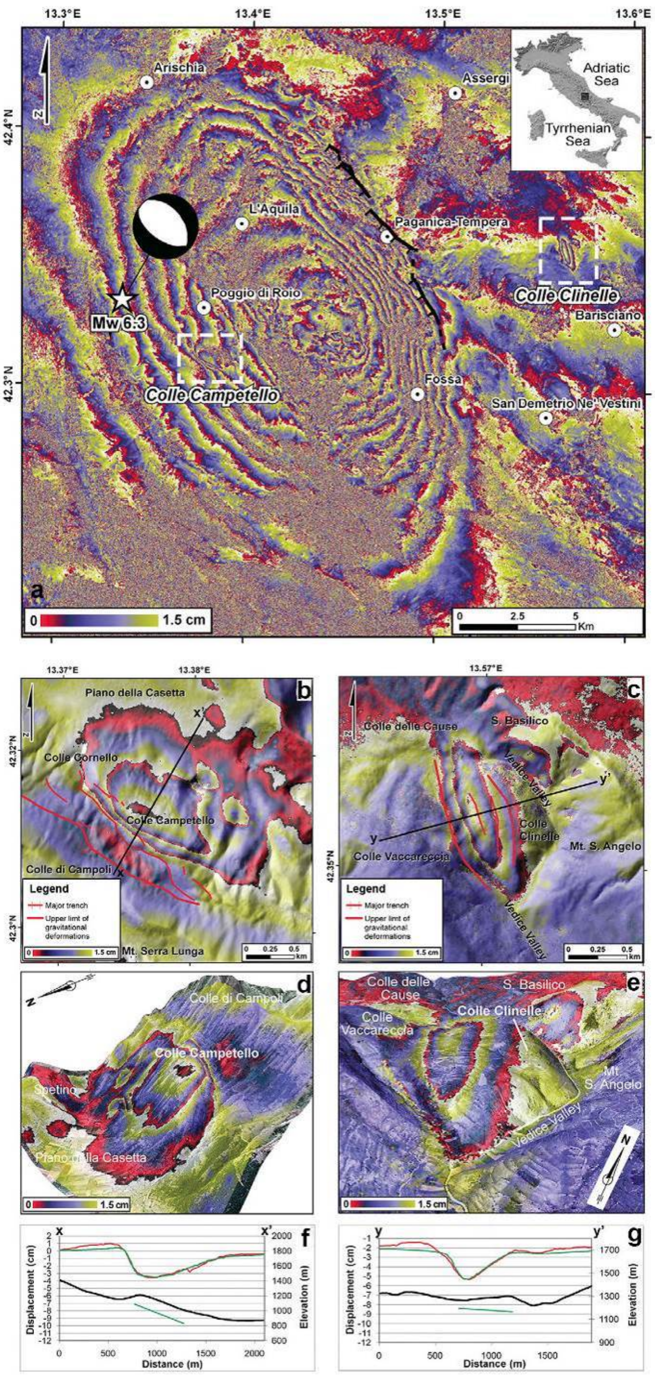

Figure 10:. (a) Full-resolution COSMO-SkyMed coseismic interferogram of the 6 April 2009 L'Aquila (Italy) earthquake area. White star is earthquake epicenter. Dashed white boxes show fringe patterns in Colle Clinelle and Colle Campetello; (b) Differential synthetic aperture radar interferometry (DInSAR) fringe pattern in Colle Campetello area after removal of seismic source displacement; each color cycle indicates ground displacement of 1.5 cm in line of sight of satellite; (c) DInSAR fringe pattern in Colle Clinelle area; (d) Three-dimensional view of interferogram in A over topography; (e) Three-dimensional view of interferogram in B over topography; (f) Ground displacement profile; trace shown in panel b; (g) Ground displacement profile; trace shown in panel c. In both profiles, topographic elevation is in black, observations are in red, unconstrained model displacement is in blue, and model displacement for the 30° dip model (panel f) and 20° dip model (panel g) are in green. Modelled dislocations are shown under topographic profiles using same colors. Figure from (Moro et al., 2011).

3.3. Post-seismic studies

While the original elastic-rebound model of the earthquake cycle envisioned steady accumulation of elastic strain punctuated by the sudden relief of this strain in an earthquake (Reid, 1910), it has become clear that relaxation of stress changes produced by a rupture in the surrounding crust and upper mantle result in observable post-seismic deformation transients.

Depending on the size of the earthquake, these post-seismic transients can be geodetically detected for up to several decades after a large event. A number of processes contribute to post-seismic deformation, including the afterslip, the poro-elastic rebound, the visco-elastic relaxation and the slope movements induced by gravity. Afterslip occurs on the same fault or faults that ruptured during the earthquake, usually immediately surrounding the rupture. Triggered slip may also occur on other faults in response to a large earthquake, sometimes at larger distances. While some of the afterslips and triggered slips occur in the form of aftershocks, they usually involve dominantly aseismic fault creep. Poro-elastic rebound is the process of fluid (mostly water) moving through the pores of rocks due to the pressure changes applied by the earthquake. Visco-elastic relaxation occurs in the upper mantle or lower crust where the rocks respond to stress changes by viscous flow that relaxes the applied stress and thus reflects the rheology of rocks at high temperatures and pressures. Slope movements happen in areas with high topographic gradients because of the geometrical perturbation caused by the coseismic ground deformation.

InSAR complements GPS and terrestrial geodetic methods used to study post-seismic deformation transients thanks to its high spatial resolution and comprehensive sampling of the deformation field (Bürgmann, 2013). Advanced time-series processing techniques have produced increasingly detailed views of the temporal patterns of post-seismic relaxation. InSAR has also captured post-seismic deformation fields of numerous earthquakes in remote regions where no other geodetic observations could be obtained (Jacobs et al., 2002; Pollitz et al., 2001; Ryder et al., 2007; Simons et al., 2002)

The 1992 M7.3 Landers earthquake was not only the first event whose coseismic deformation field was observed by InSAR, but InSAR also illuminated the post-earthquake deformation transients following this event with unparalleled resolution (Fialko, 2004; Massonnet et al., 1994; Massonnet et al., 1996; Peltzer et al., 1996, 1998; Pollitz et al., 2002). Post-seismic interferograms revealed deformation associated with a M5.4 aftershock, shallow triggered slip on a fault segment just to the south of the co-seismic rupture, broadly distributed deformation associated with deep seated shear, and a strong deformation signal localized near stepovers in the rupture (Peltzer et al., 1996, 1998). The analysis of the deformation in the fault stepovers led to the discovery of poro-elastic rebound as an important post-seismic relaxation mechanism. Post-seismic subsidence occurred in restraining (left) stepovers and uplift in releasing steps of the rupture, opposite to what might be expected if slow fault slip is the primary shallow post-seismic mechanism. This pattern can be explained if fluid in the crust flows in response to coseismic pore-pressure changes. Interestingly, evidence for poro-elastic rebound has been detected with InSAR following some large earthquakes (Jacobs et al., 2002; Jónsson et al., 2003) but not after some others (Barbot et al., 2008), suggesting that hydrological conditions vary widely among tectonically active regions.

Thanks to its high spatial resolution, InSAR has given valuable contributions to the study of shallow post-seismic afterslip transients that produce sharp offsets along and near the coseismic rupture. Even in areas with dense GPS network deployments, this added spatial coverage allows for much improved determination of the afterslip distribution. In the case of the 2004 Mw 6.0 Parkfield earthquake, which occurred along a partly coupled section of the San Andreas fault, it was found that the moment release from afterslip greatly exceeded that of the coseismic rupture (e.g., (Johanson et al., 2006).

Reale et al. (2011) and D'Agostino (2012) carried out a detailed SBAS time series analysis of COSMO-SkyMed measurements of deformation following the 2009 M6.3 L'Aquila normal-faulting earthquake in Italy (Figure 11). Similarly to the spatial pattern observed in the Parkfield afterslip distribution, the post-seismic slip following this event surrounded the main co-seismic rupture asperity. The time series analysis shows that the rapidly decaying afterslip transients of the L'Aquila earthquake have a decay constant of 20-40 days, similar to what was found for the Parkfield, Nima and other earthquakes that produced shallow afterslip transients.

InSAR monitoring of deformation following the 2003 Bam, Iran, earthquake allowed for the documentation of yet another shallow post-seismic process that accompanied afterslip and poro-elastic rebound (Fielding et al., 2009a). A narrow zone of subsidence right above the fault patch of greatest co-seismic slip at depth can be explained by the recovery of damage and dilatancy produced during the earthquake. SBAS time series analysis of > 100 interferograms shows that healing and compaction of coseismic dilatation in the upper kilometer of the fault zone evolved logarithmically over the 3-year observation period (Figure 12).

Motagh et al. (Motagh et al., 2014) exploited InSAR data provided by ALOS, Cosmo-SkyMed and TerraSAR-X to study the post-seismic deformation following the 2010 Darfield (New Zealand) earthquake. A subsidence signal peaking at about 5 cm was detected in the epicentral area of the Charing Cross fault during the first ~6 months after the event. In addition, a right-lateral shear along the eastern end of the Greendale Fault, highlithing a postseismic afterslip process.

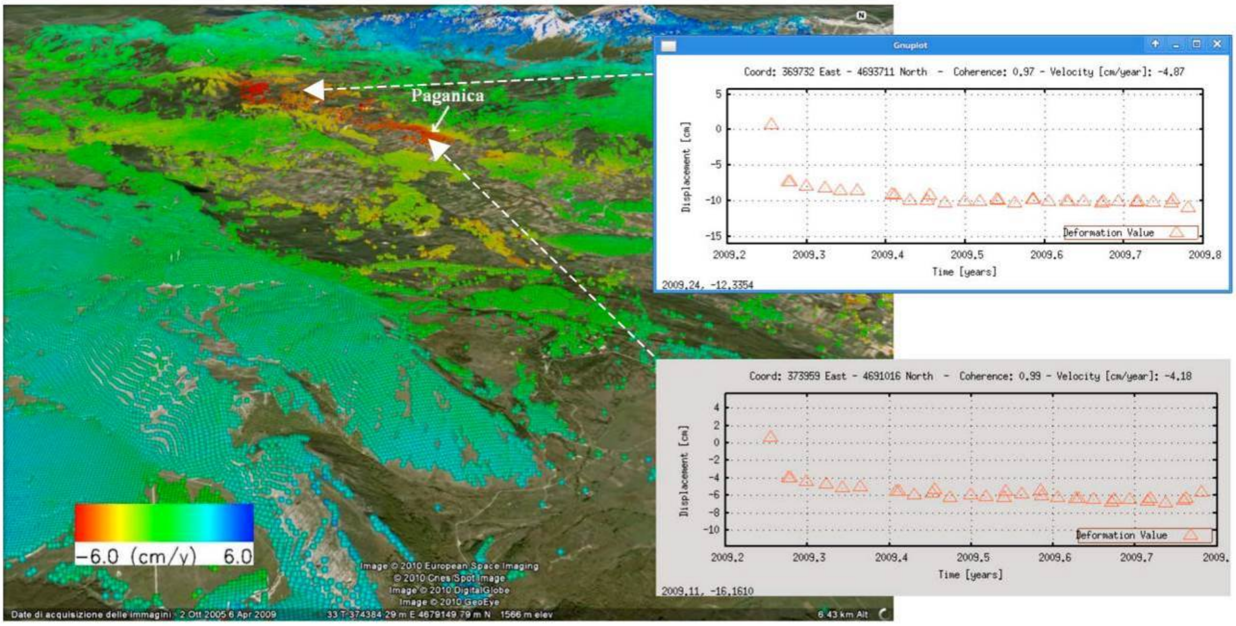

Figure 11: Mean velocity estimated by the post-seismic acquisitions following the L'Aquila earthquake at low resolution obtained by the Two-Scale Interferometric Analysis (TSIA) technique. The time series of two relevant pixels shows the line-of-sight surface displacement versus time, starting from pre-seismic acquisition of April 4, 2009. The post-seismic deformation shows an exponential decay going from about −6 cm to −10 cm (Reale et al., 2011).

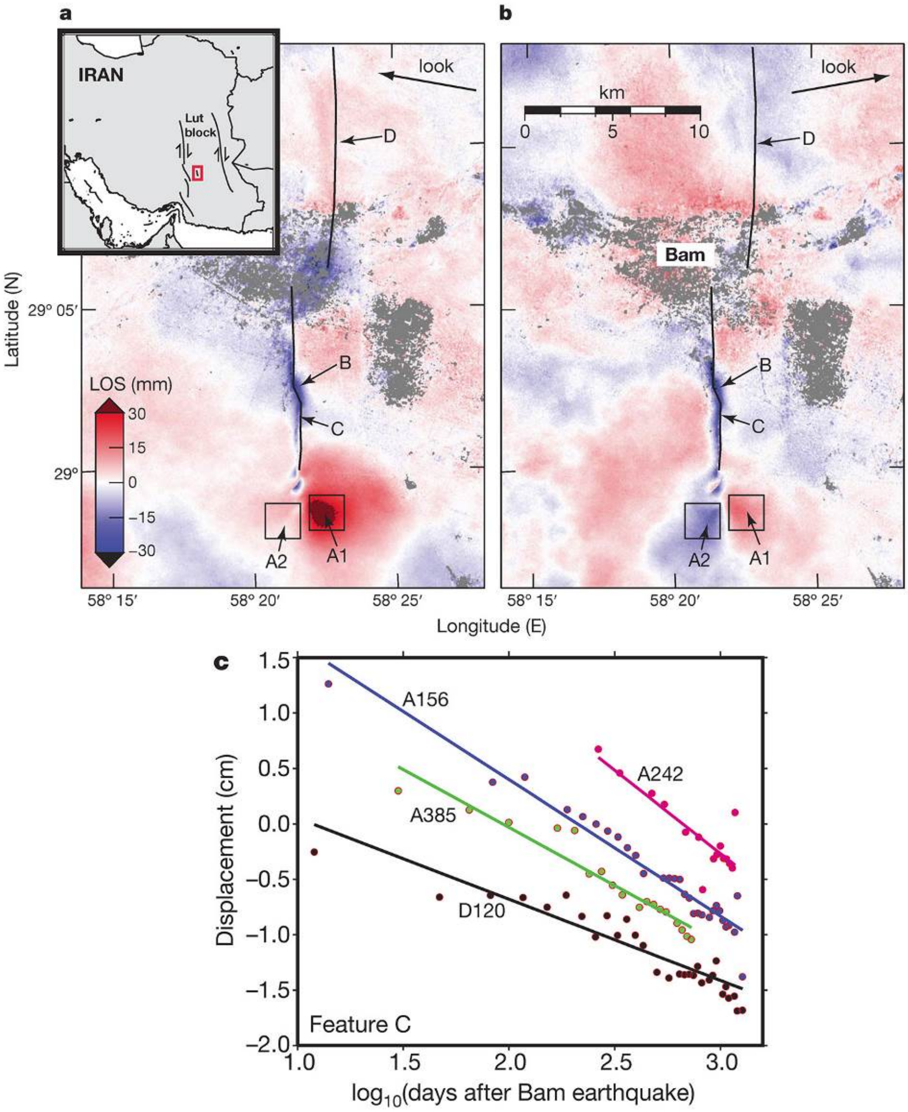

Figure 12: Post-seismic surface deformation after the 2003 Mw 6.6 Bam, Iran, earthquake: (a) and (b), maps from two Envisat tracks in radar line-of-sight showing total displacement between 12 and 1,097 days after the 26 December 2003 earthquake. (c) time series of subsidence south of fault bend (difference between polygon C and adjacent areas) interpreted as recovery of co-seismic dilatancy in the shallow fault zone. From (Fielding et al., 2009b).

Triggered slip on faults away from the coseismic rupture had been observed before the advent of InSAR, but the dense spatial coverage of InSAR images has shown that this is a common phenomenon. The first InSAR observations of triggered slip were made after the 1992 Landers earthquake (Peltzer et al., 1994). Other examples of triggered slip include the 1999 Izmit, Turkey earthquake (Wright et al., 2001), 1999 Hector Mine, California earthquake (Fialko et al., 2002; Sandwell et al., 2002), 1994 Double Spring Flat, Nevada earthquake (Amelung and Bell, 2003), 1998 Fandoqa earthquake in Iran (Fielding et al., 2004), and 2010 El Mayor-Cucapah earthquake in Baja California, Mexico (Rymer et al., 2011; Wei et al., 2011). Only for the California faults we have detailed timing information on the triggered slip. In all of these examples, the InSAR measurements show that the triggered slip occurred only on the shallowest part of faults, which confirms theories that the upper ~1 km of faults have very low strength and slip with relatively small applied stress changes (Marone, 1991). The question remains open whether triggered slip is caused by the transient dynamic stresses as the earthquake waves pass or by the static stress change due to the main fault slip.

The Landers earthquake was followed seven years later by the 1999 Mw 7.1 Hector Mine earthquake, which produced a pattern of post-seismic surface deformation that has been used to suggest that viscoelastic relaxation in the upper-mantle dominated over lower-crustal afterslip or flow following this event (Pollitz et al., 2001). The earthquake produced a far-reaching deformation pattern with a quadrant uplift pattern opposite to that expected for localized shear beneath the earthquake rupture.

Biggs et al. (2009) examined the post-seismic deformation field of the 2003 Mw 7.8 Denali earthquake in Alaska measured with InSAR and GPS to confirm that the principal relaxation process must have occurred in the uppermost mantle to explain peak transient displacements at 50-km distance on either side of the rupture (Figure 13). A viscosity ratio of at least 5 between the lower crust and upper mantle is required to explain the relatively modest contribution of relaxation in the lower crust (Biggs et al., 2009). The delayed initiation of slope movements, ranging from hours to days after the earthquake, has been sometimes observed in the past (Agnesi et al., 2005; Keefer, 2002; Lacroix et al., 2014). More recently, a detailed Persistent Scatterer Pair (PSP) time series analysis of a 16 months long COSMO-SkyMed dataset following the 2009 Mw 6.3 L'Aquila earthquake revealed the existence of post-seismic ground subsidence in the mountainous rocky area of Mt. Ocre ridge, contiguous to the sedimentary plain that experienced the coseismic subsidence. In the Mt. Ocre ridge, widespread morphological elements associated with gravitational spreading were previously mapped. Numerical analyses performed with the finite element method found that part of the observed post-seismic displacement is caused by the plastic deformation of the rocky material under gravitational loading. Such plastic deformation produced a lateral-spreading mechanism of the ridge that justifies the observed landforms (Figure 14) (Albano et al., 2015a).

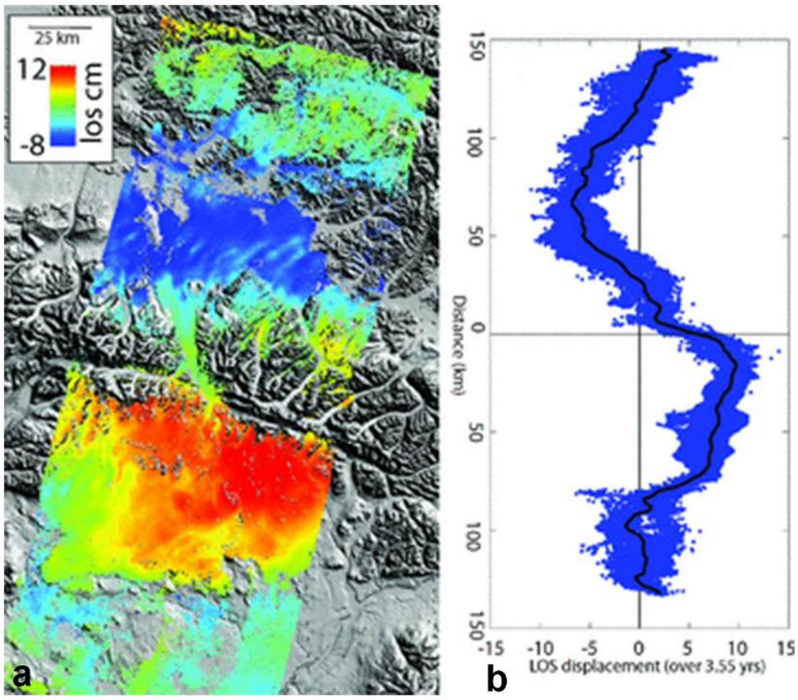

Figure 13: Left: stack of four interferograms processed from acquisitions in the summers of 2003 and 2004 across the central rupture zone of the 2002 Mw 7.8 Denali earthquake, showing a peak range change of 2–3 cm in the satellite line-of-sight over the 1-yr time period. Right: Range-change profile (blue data points with black line indicating average values) perpendicular to the Denali fault taken from the entire image. Peak displacement in the north is located 50–60 km from the fault. From (Biggs et al., 2009).

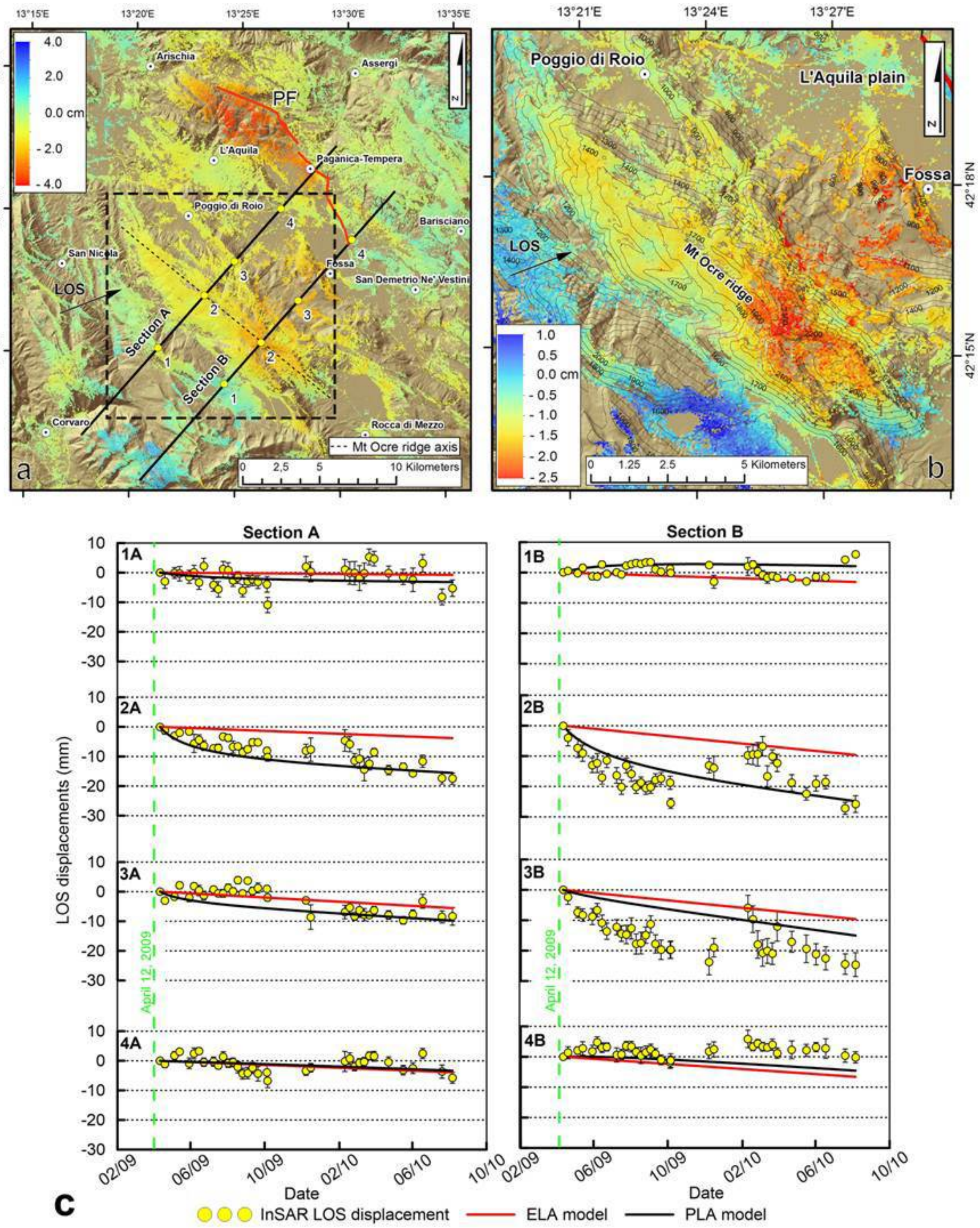

Figure 14: (a) Line of sight post-seismic displacement map after the 2009 L'Aquila earthquake. The InSAR dataset covers a time interval between April 12, 2009 and August 6, 2010. (b) Detail of the post-seismic displacement affecting the Mt Ocre ridge area (black box in Fig. 11a). (c) Time series of the observed and modelled LOS displacements time series for points on sections A and B in Fig. 11a. The black line represents the result of elastoplastic model (PLA), while the red line the elastic model (ELA). From (Albano et al., 2015a)

3.4. Interseismic studies

InSAR has proven to be of great value in observing strain and slip along faults that occurs in the time period between earthquakes thanks to its improving precision and temporal resolution. Most faults are “locked” between earthquakes, and the surface observations surrounding them reflect steady motions of the lower crust and mantle as strain accumulates in the elastic upper layer. A few faults exhibit interseismic creep at the surface, because some portion of the long-term slip is accommodated by steady sliding on the shallow fault interface. For the most part, interseismic deformation appears to be fairly time invariant. However, in a few cases, slow deformation transients have been observed, probably due to deep slip on the fault interface.

The rates of interseismic deformation are typically much smaller than those occurring during earthquakes or in the post-seismic period and result difficult to measure. This is the case of the North Anatolian Fault having a long-term slip rate of ~20 mm/yr (Kozaci et al., 2007), which is relatively high compared to most active faults. As the North Anatolian Fault is roughly parallel to the ground range for ERS and Envisat acquisitions, with incidence angles of 23° from the vertical at the scene center, the fault-parallel slip causes therefore motion of only ~8-10 mm/yr in the satellite LOS. It is obvious that in order to maximize the interseismic signal in any interferogram, it would be preferable to observe for a long period. However, it may happen that for many places, including the North Anatolian Fault, coherence drops off within a few months to years. Therefore, noise from orbital error and the atmosphere disturbances return single interferograms generally insufficient to measure interseismic deformation around locked faults.

InSAR measurements of strain accumulation have had the most significant scientific impact in more remote locations with sparse GPS networks, while have less value in regions with high GPS density. An example is the Tibet, cut by several major strike-slip faults, which slip in response to the ongoing collision of India with Asia. In the “pre-SAR satellite” era, the slip rate on the Karakoram and Altyn Tagh Faults was thought to be relatively high, 2-3 cm/yr, similarly to the slip rate on the Main Frontal Thrust of the Himalayas (Tapponnier et al., 2001). InSAR observations have ruled out such high slip rates for the Karakoram Fault, that is currently constrained to accumulate strain at a rate consistent with a long-term slip rate of no more than 7 mm/yr (Wang and Wright, 2012; Wright et al., 2004). In addition, the Altyn Tagh Fault has a slip rate of ~11 mm/yr (Elliott et al., 2008; Jolivet et al., 2008) and the Xianshuihe, Manyi and Haiyuan Faults in eastern Tibet have slip rates measured with InSAR of 3-10 mm/yr (Bell et al., 2011; Cavalie et al., 2008; Wang et al., 2009). In addition to the slip on the major faults, InSAR data have been used to argue that there is significant internal deformation within the plateau, some of which occurs on unmapped, smaller fault systems (Taylor and Peltzer, 2006; Wang and Wright, 2012).

Another example of successful use of InSAR data has been mapping near-surface fault creep (Behr et al., 1990; Bürgmann et al., 2000; Cakir et al., 2005; Funning et al., 2007; Hsu and Bürgmann, 2006; Johanson and Bürgmann, 2005; Rosen et al., 1998). Since the deformation is localized at the fault trace and it causes sharp discontinuities in interferograms, fault creep is somewhat easier to be detected than strain from fully locked faults. A well-known example is the San Francisco Bay area of California, where InSAR allows detailed spatial variations of fault creep to be mapped in the Hayward Fault (Bürgmann et al., 2000; Schmidt, 2005; Schmidt et al., 2005). A time-dependent model of creep on the Hayward fault obtained from time series of 18 years of ERS and Envisat acquisitions (with a total of 102 epochs) reveals significant variations in slip rate on creeping sections of the fault surrounding a large locked asperity that slips in M~7 sized earthquakes (Shirzaei, 2013). In a recent time series analysis of the Parkfield section of the San Andreas Fault, (De Michele et al., 2011) showed that surface creep varied in space and time between 1993 and 2004.

Efforts to improve our understanding of the physical mechanisms controlling the occurrence of earthquakes should focus on events that alter the stress state. This is the case of earthquake swarms driven by aseismic creep. Earthquake swarms are sequences of earthquakes clustered in time and space, lacking a clear mainshock (Hill, 1977; Mogi, 1963; Sykes, 1970), covering an unusually large spatial area relative to their total seismic moment release, and failing to decay in time according to standard aftershock scaling laws (Roland and McGuire, 2009). Swarm-like earthquake sequences are observed in a diverse range of geological settings including volcanic (Bianco, 2004); (Guglielmino et al., 2011) and geothermal regions (Dziak, 2003) as well as along transform plate boundaries and active rift zones (Baer, 2008; Pallister, 2010), where earthquake swarms are associated with surface fault scarps and extensional cracks (Pollard et al., 1983; Rubin and Pollard, 1988). Many earthquake swarms appear to be shallow sequences along normal faults or in geothermally active areas (Vidale, 2006), suggesting that pore fluid diffusion plays a role in their spatio-temporal evolution. There are a small number of swarms for which a surface deformation signal has been captured (Mrlina, 2008) including with InSAR (Lohman and McGuire, 2007). The InSAR measured deformation associated with these seismic swarm shows that much of the slip accompanying the seismicity was aseismic in some cases (Wicks et al., 2011) and with substantial seismic slip in others. In a recent case study in Greece (Peloponnese Peninsula), InSAR has been applied to follow the migration of the seismicity and related changes in surface displacement field in space and time (Kyriakopoulos C., 2013). Here also, the amount of surface displacement greatly exceeds that released by the earthquakes (including Mw 4.8, 4.6, and 4.7 events) of the sequence (Figure 15).

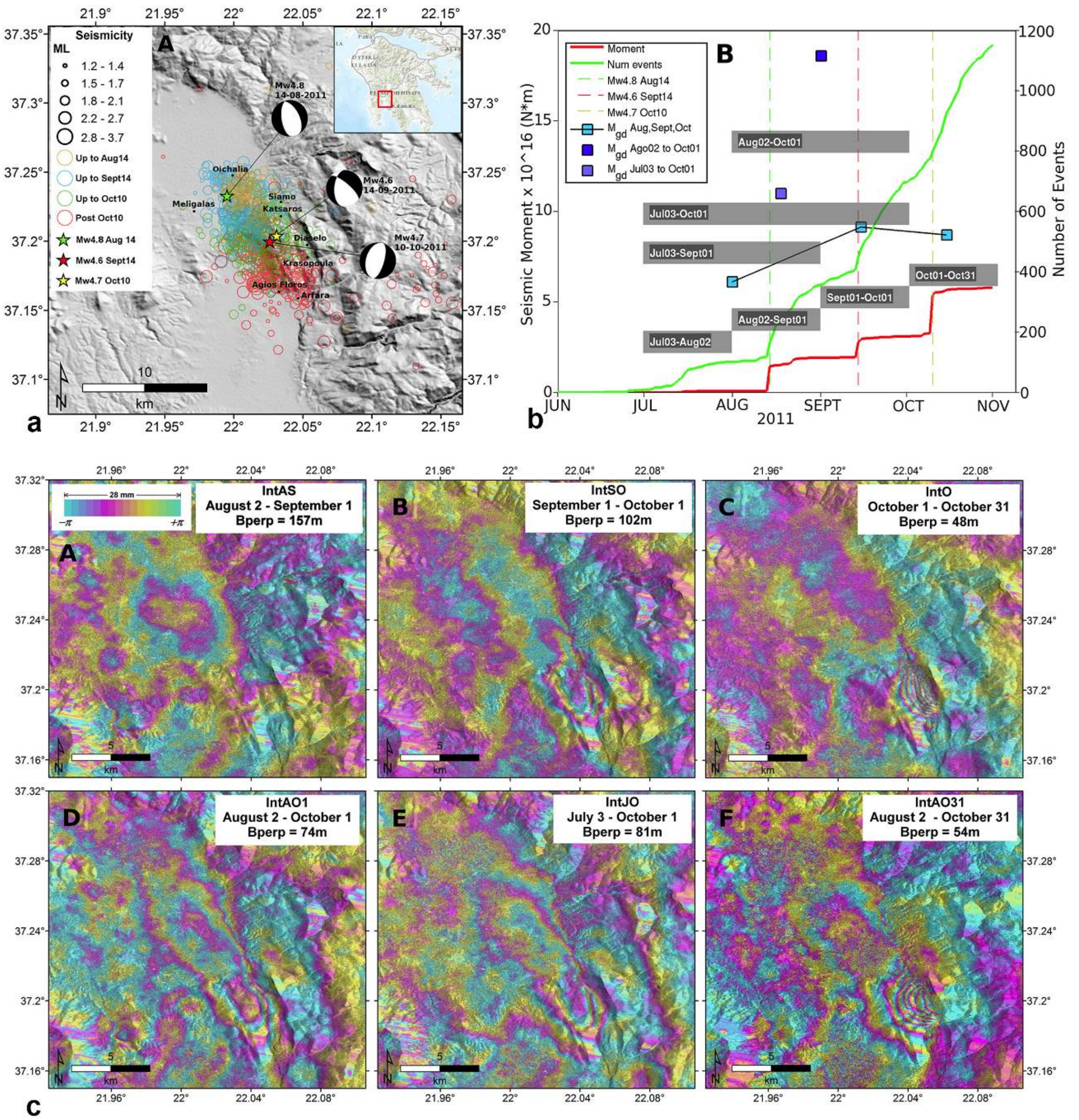

Figure 15: (a) Observed seismicity and swarm migration: the three mainshocks of the seismic swarm are dated August 14 (green star), September 14 (red star) and October 10 (yellow star). The seismicity has been clustered in time in four patches: three respectively before each mainshock, the last one after October 10 shock; (b) Seismic moment evolution and available SAR images: seismic moment (red line) increases parallel with the number of shocks. Geodetic moment aggregated for each month; (c) Differential Interferograms relevant to the swarm evolution. From (Kyriakopoulos C., 2013).

Satellite geodetic data have been responsible for a remarkable discovery in recent years, that faults can experience episodic tremor and slip: sudden slow creep events, associated with non-earthquake seismic signatures (Rogers and Dragert, 2003). Although the primary source of observations has come from continuous GPS observations, InSAR has been useful for mapping the spatial extent of deformation occurring in several of these transients. One such slow slip event that occurred in 2006 on the Guerrero subduction interface in Mexico has been mapped with InSAR (Bekaert et al., 2010; Hooper et al., 2011). It has proved easier to find slow slip events (or silent earthquakes) on shallow crustal faults. For example, (Lohman and McGuire, 2007) detected deformation associated with a seismic swarm in the Salton Trough in 2005. Although there was intense earthquake activity, the seismic moment release was insufficient to explain the observed deformation. Instead, it seems likely that the earthquakes were triggered by aseismic slip on the fault (Wei, 2009). (Furuya and Satyabala, 2008) detected a slow earthquake on the Chaman Fault Zone in Afghanistan. In this case, the slip followed a M5.0 earthquake, and lasted for more than a year, causing deformation along 50 km of the fault.

4. The knowledge of volcanic processes

An InSAR image can map deformation with a high level of spatial resolution (a few to tens of meters) and centimeter to subcentimeter precision during the time interval separating the acquisition of two SAR images (Lu, 2002; Massonnet and Feigl, 1998). Multiple InSAR images spanning a variety of time intervals can be used to characterize transient deformation (Feigl et al., 2000; Lu, 2003). InSAR imagery is particularly valuable for monitoring the deformation of volcanoes having remote locations and, as a consequence, no other instrumentation. Interpretations of InSAR images are especially useful at volcanoes where crustal displacements indicate magmatic activity. The observed deformation alone is interesting, but more importantly, it can be used to infer subsurface processes that cannot be directly observed. Therefore, routine geodetic monitoring is one of the key tool to understand the state of activity of a volcano. Indeed, analysis of the background state and detection of variations of the monitored parameters are needed for the definition of the volcano hazard. Mechanical modeling, constrained by InSAR imagery, is a powerful tool that can quantify the spatial and temporal deformational mechanisms within a volcano. The ultimate goal in volcanology is a refined understanding of the interaction of magmatic and hydrothermal reservoirs, with a focus on the threatening phenomena as, for instance, the surface effects of resurgence and tectonic dynamics (e.g., Pernicana fault at Mt. Etna), the switch from non-eruptive to eruptive unrest (e.g., Campi Flegrei, Santorini) or the possible transition from obstructed to open-conduit conditions (e.g., Somma-Vesuvius, volcanoes in Island, Fogo). In case of open-vent volcanoes, degassing, rate of magma heat loss and eruption rates are balanced. Some of the typical characteristics are small frequent eruptions, minimal seismicity and ground deformation before eruptions. Generally, ground surface expands before eruptions due to pressure increase within a shallow magma chamber caused by upward magmatic movements. During and after the eruption has ended, deflation occurs in the volcano (Bignami et al., 2014). Patterns and rates of surface displacement can be used to obtain the depth and rates of pressure increase within the magma chamber, as well as size and shape of the center of deformation, which may be related to the top of the magma chamber (Dvorak and Dzurisin, 1997).

4.1. Unrests (Closed conduit)

Since its last eruption in 1950, Santorini volcano (Greece) remained in a dormant state. This is also evidenced for the period 1992–2010 by the gradual deflation signal over Nea Kameni as measured by ERS-Envisat SAR dataset with low rates of about 5–6 mm/yr (Figure 16), as well as by the absence of seismic activity within the caldera (Foumelis et al., 2013). At the beginning of 2011 the volcano showed signs of unrest with increased microseismic activity and significant ground uplift, reaching 14 cm within a year (2011 March–2012 March), according to InSAR time-series (Figure 17). ALOS PALSAR data indicate the onset of the phenomenon in early 2010 where an aseismic pre-unrest phase of increased subsidence (1–3 cm) preceded the uplift. Joint inversions of SAR and GPS velocities constrained a spherical magmatic source located offshore at about 1 km North of Nea Kameni and ~3.5 km depth. The geodetic data inversion gives insights to the volume variation rate, estimated as ~6 10^6 m^3/yr. Satellite monitoring from Envisat and RADARSAT-2 attested also a gradual slowing trend in the rate of inflation during 2012, decreasing the volcanic risk estimate of the touristic island of Santorini.

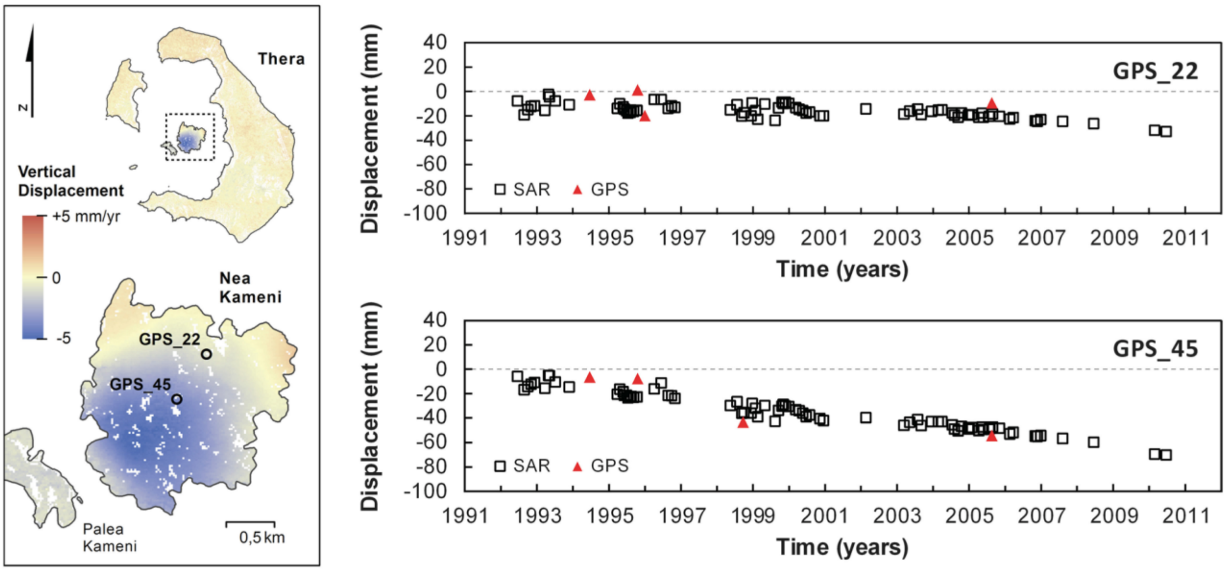

Figure 16: Vertical displacement time-series for the rest period (1992–2010) from combination of ascending and descending SAR acquisitions at GPS sites. The systematic linear motion trend at the area of the maximum observed subsidence on Nea Kammeni is evident. From (Foumelis et al., 2013).

Campi Flegrei (CF) caldera is a volcanic district in southern Italy, nearby the city of Naples. Two main eruptions, dated 35 ka and 15 ka ago, have been predominantly responsible for its formation (Rosi et al., 1993). The area is characterized by one of the highest volcanic risk worldwide, due to the density of inhabitants (1800/km^2) and the persistent activity of the closed conduit system. CF caldera (Italy) was affected by a new unrest phase during 2011–2013. COSMO-SkyMed data mapped the deformation field, obtaining displacement rates reaching 9 cm/yr in 2012 in the caldera center (Trasatti et al., 2015). Figure 18 shows cumulative displacement maps 2011-2013, characterized by a semicircular pattern centered in the Pozzuoli harbor (Figure 18a and b). In addition to InSAR, GPS data from 14 stations of the NeVoCGPS network have been also employed (De Martino et al., 2014). The horizontal GPS vectors and the computed E-W InSAR data reveal a quite radial pattern centered in Pozzuoli (Figure 18c). The computed vertical InSAR data measure 16 cm uplift in Pozzuoli and disclose a slightly subsiding far field belt undetected by GPS (Figure 18d). The time series of RITE (in Pozzuoli) and SOLO (in Solfatara) show a good agreement between the vertical GPS and InSAR data (Figure 18e and f). The resulting data set is fitted in a geophysical inversion framework obtaining a sill-like source lying at ~5km depth. The driving mechanism is ascribable to magma input into the source of the large 1982–1984 unrest (since similar source characteristics were inferred) that generates initial inflation followed by additional shear slip accompanying the extension of crack tips. The history and the current state of the system indicate that CF is able to erupt again, and the advanced techniques adopted provide useful information for short-term forecasting.

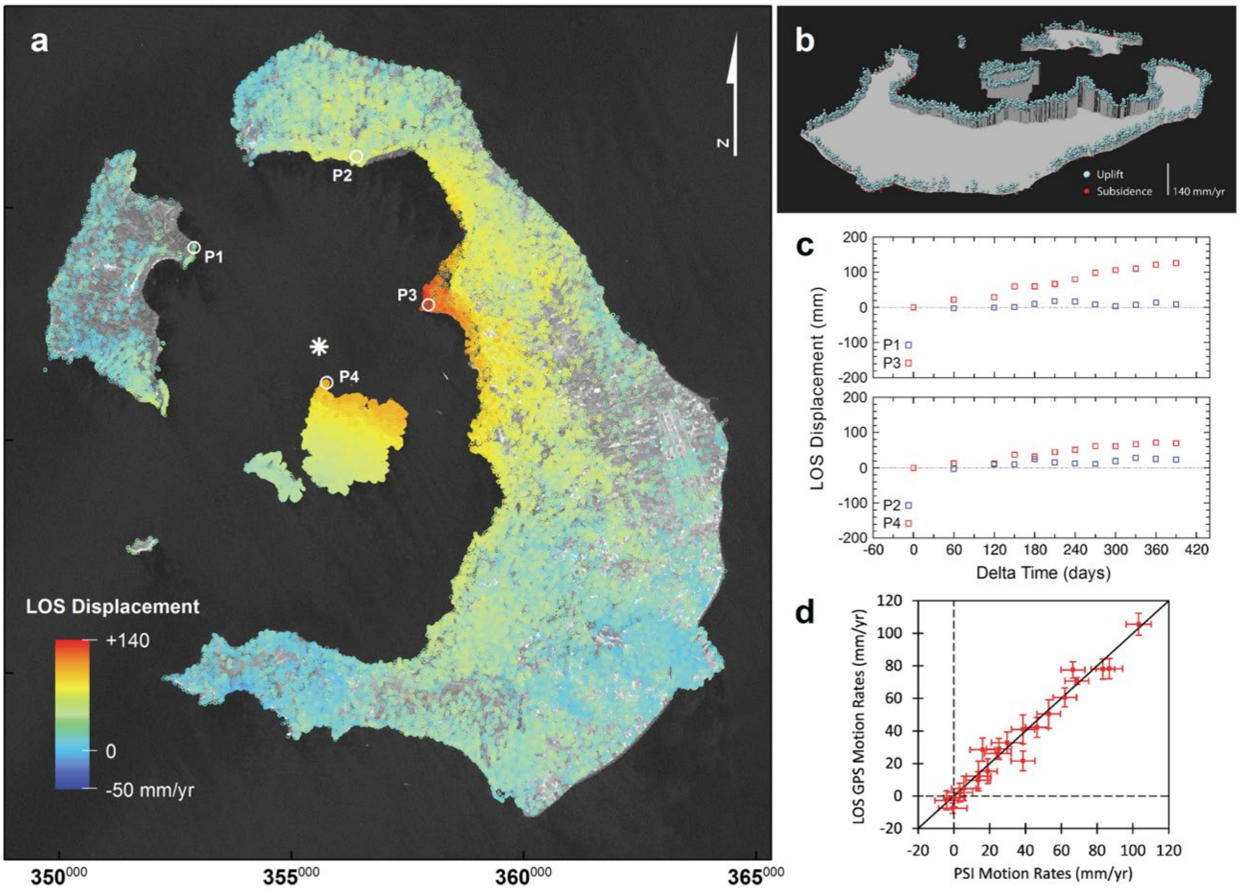

Figure 17: (a) PSI LOS displacement rates from ENVISAT data (2011 March–2012 March) showing the radial inflation pattern caused by the volcanic unrest, (b) perspective 3-D view of the point targets along the coastline of Santorini, (c) deformation histories of selected point targets and (d) correlation between GPS motion rates projected into the LOS geometry and PSI results. From (Foumelis et al., 2013).

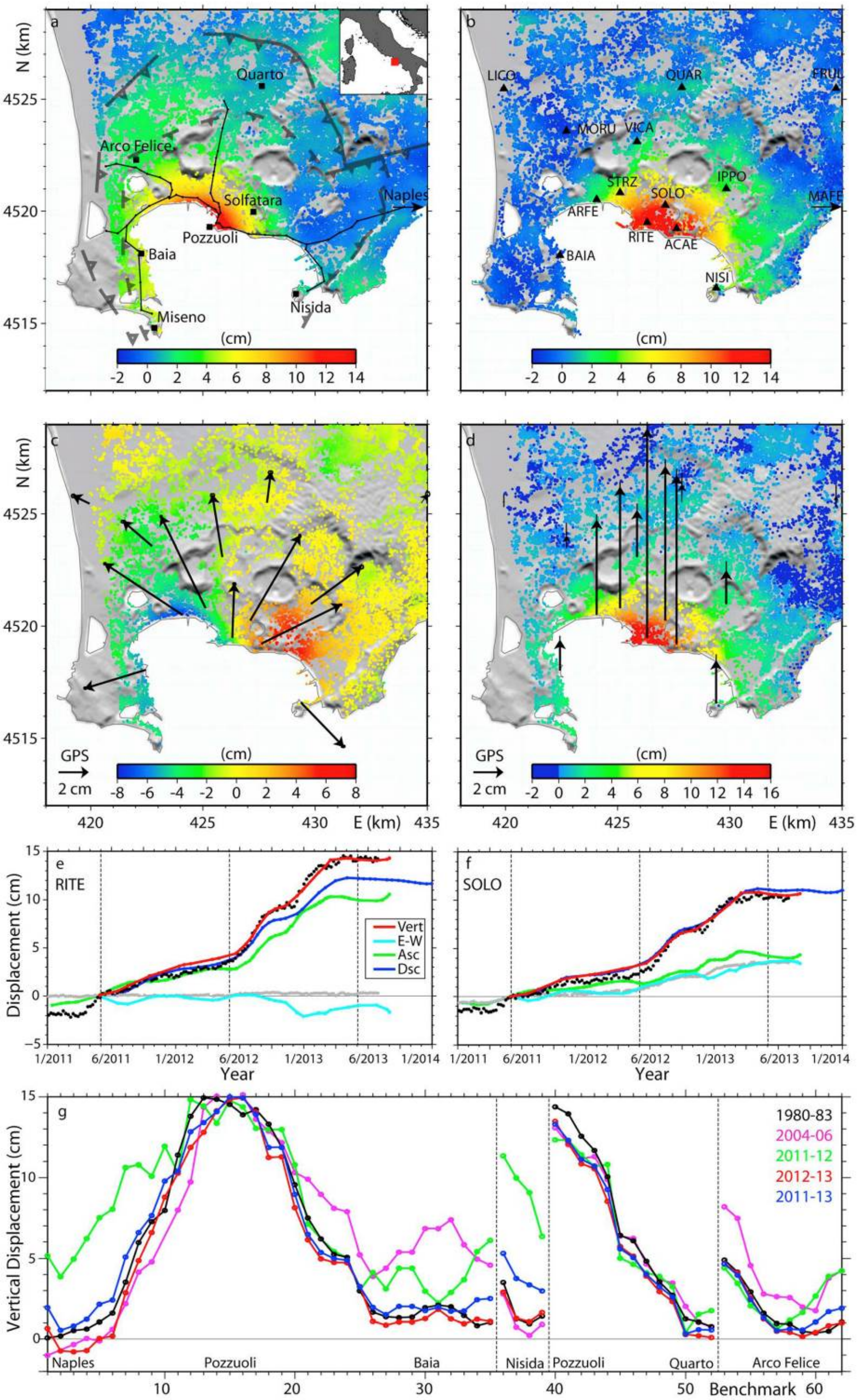

Figure 18. LOS cumulative displacements in (a) ascending and (b) descending orbits from CSK between 31 May 2011 and 5 May 2013. In (a) the outer/inner rims of the CF caldera are shown with open/full triangles, while the black lines are the 1980s leveling routes. In (b, the triangles are the GPS stations. (c) E-W and (d) vertical displacements computed in the common pixels of (a) and (b). Horizontal and vertical GPS components are reported in Fig. 1c and 1d, respectively. UTM-WGS84 projection, zone 33. In (e) and (f) time series at the GPS stations RITE and SOLO (vertical, black dots and E-W, grey dots) and corresponding InSAR data. Vertical displacement patterns along the 1980s leveling routes during past and present unrests, normalized to the maximum value observed during 2011–2013. From (Trasatti et al., 2015)

4.2. Pre-eruptive and eruptive dynamics

An eruption started on Fogo Volcano (Cape Verde) on the 23 November 2014, almost 20 years after the previous one. A pair of Sentinel-1 images along ascending path, dated November 3 and November 27, 2014 were used to investigate deformations occurring on the caldera and volcano edifice during the first sin-eruptive phase (Figure 19) (Albano et al., 2015b). Actually, this is the first case of InSAR technique application to a pair of images acquired in the very new mode of Sentinel-1, i.e., the Terrain Observation with Progressive Scans SAR (TOPSAR) mode. The resulting map shows two main patterns located WNW and E with respect to the volcano peak (Pico do Fogo). The western unwrapped pattern reaches a maximum LOS deformation of about 11 cm towards the satellite, and the eastern side shows a displacement with a minimum close to -6 cm. These data were useful to carry out source inversion in order to simulate the effect of the feeding dyke on the surface displacements. It results that a dyke of 1.5 km x 2.5 km opened ~80 cm at a very shallow depth, with a total volume change amounting to ~3 10^6 m^3.

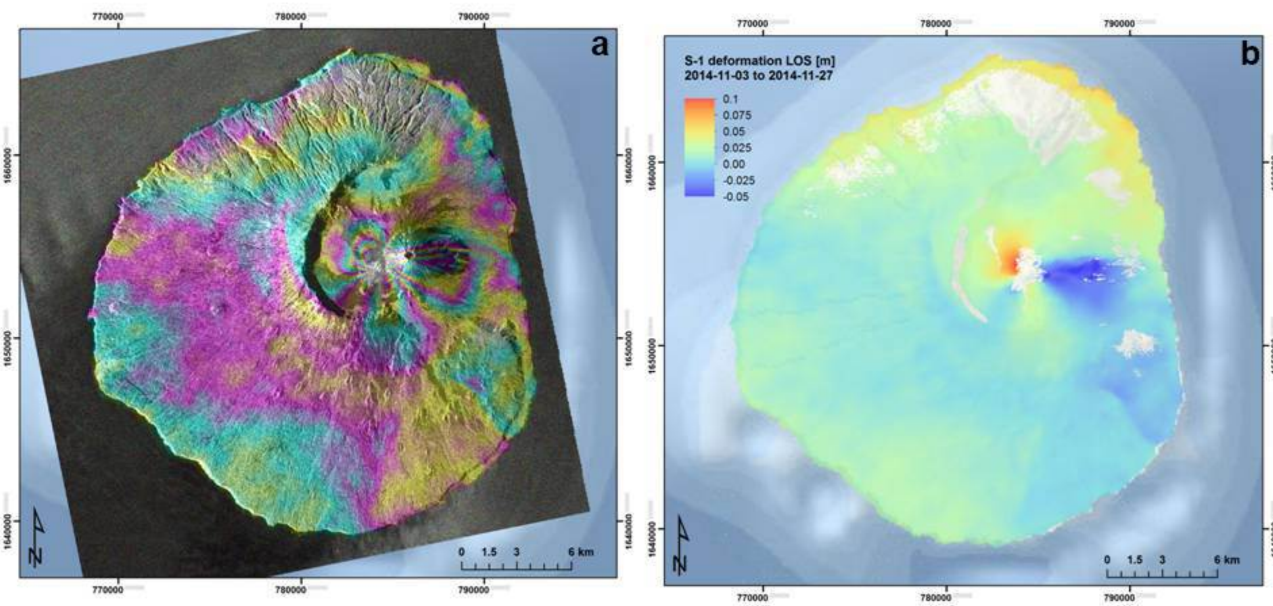

Figure 19. Sentinel-1 interferogram generated by exploiting an ascending image pair. Panel (a) reports the wrapped interferograms, panel (b) shows the corresponding deformation map along the LOS retrieved by means of minimum most flow unwrapping. From (Albano et al., 2015b).

4.3. Dynamics of tectonic features

Mt. Etna is a classical open-conduit volcanic system dominated by nearly persistent activity, generating both effusive and explosive eruptions. Space agencies have sun background missions for Mt. Etna over a long time (since the 1980s), so that the current EO data base, for both SAR and optical data, is probably the largest in the world for active volcanoes, including EO time series starting from 1984 (LANDSAT) and 1992 (ERS), respectively. All current EO missions comprise the collection of data and new missions (e.g., Sentinel) offer possibilities to increase the number of parameters measured with high accuracy from space (e.g., deformation, gas emissions, thermal structures).

Neri et al. (Neri et al., 2009) presented a study of 15 years of InSAR observations at Mt Etna (Fig. 20). The InSAR analysis (based on SBAS presented above) resolves the space-time evolution of the surface deformation. In particular, they processed 107 ascending and 102 descending SAR data acquired by the ERS-1/2 and ENVISAT sensors, for the 1992–2006 period. From these SAR data they computed 283 interferograms from the ascending orbits and 289 from the descending ones. At this stage, the availability of InSAR deformation time series relevant to both the ascending and descending LOS enables separation of the mostly Vertical (V) and East–West (E–W) components of the displacements. This kind of dataset constitutes an exceptional opportunity to monitor the long-term behavior of a volcano, as well as a significant improvement from previous Mt. Etna InSAR studies focused on deformation maps from single interferograms. The joint interpretation of InSAR and volcanological data allows to distinguish two volcano-tectonic behaviors associated to the 1993–2000 (general inflation of Mt Etna volcanic edifice, magma emplacement at shallower depths) and 2001–2005 (vertical propagation of a dyke responsible of the 2001 2002–2003 eruptions) time intervals. These results clearly show that the joint interpretation of volcano deformation and stored magma rates may be crucial for identifying impending volcanic eruptions and tectonic activity.

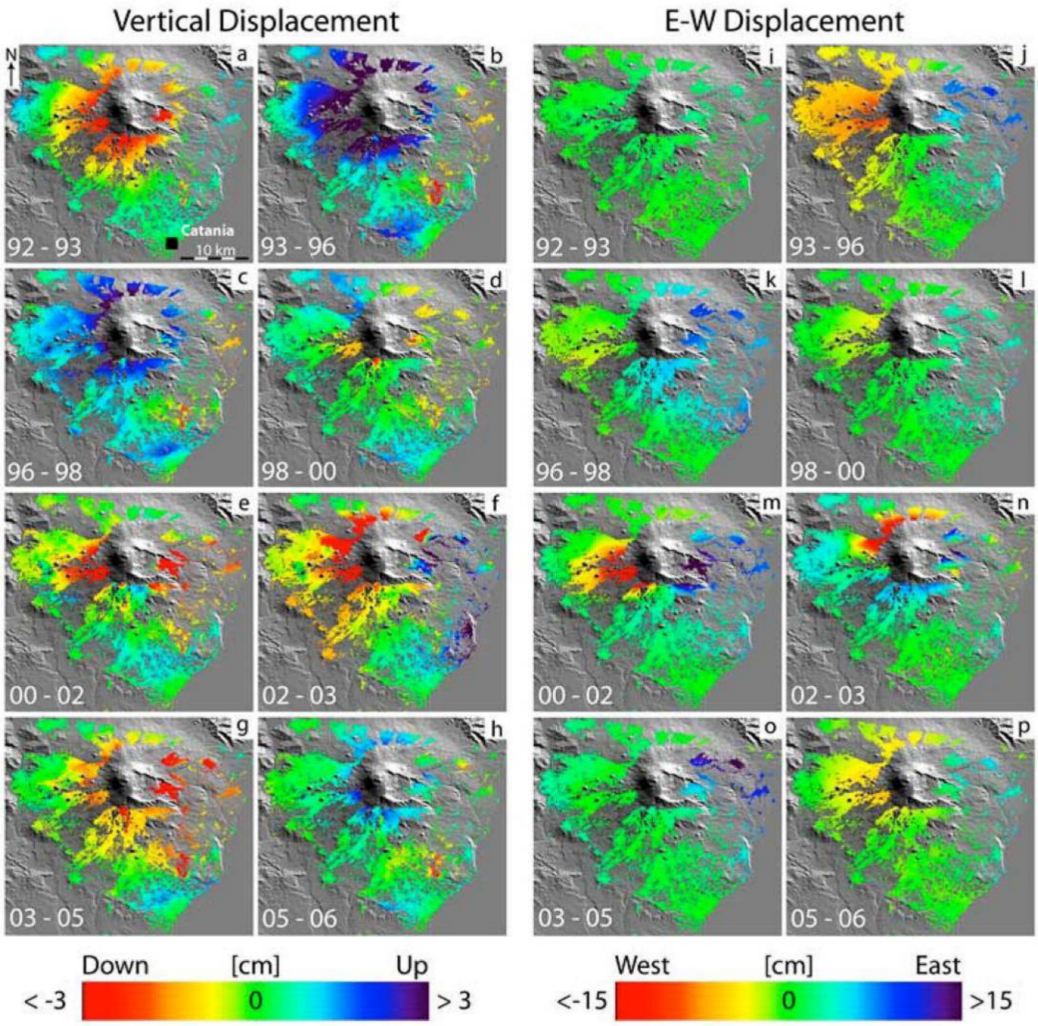

Figure 20. Deformation maps, referring to coherent zones, showing one-year average displacement variations retrieved by applying the SBAS-InSAR technique to the ERS-ENVISAT SAR dataset (mid 1992-end of 2006). Maps present (a)–(h) vertical and (i)–(p) east–west deformation components and are spatially referenced to the highlighted pixel located in Catania (black box in a). From (Neri et al., 2009).

Considering the interval between 1993 and 1997, InSAR results show that the inflation of the volcano edifice is accompanied by instability of the eastern flank (Trasatti et al., 2009). In this case, the high quality Envisat InSAR data play a key role in defining the northern limit of the flank instability, clearly represented by the Pernicana fault (Figure 21). This feature was not clearly detected by GPS and EDM measurements, despite the high number of benchmarks. Another important aspect regards the modeling, once the sliding is defined and accounted for in the inversion models, the inferred source location changes sensibly (source center shifts ~1 km SE and its strength decreases by ~20 per cent w.r.t. the case of the magmatic source alone and no sliding).

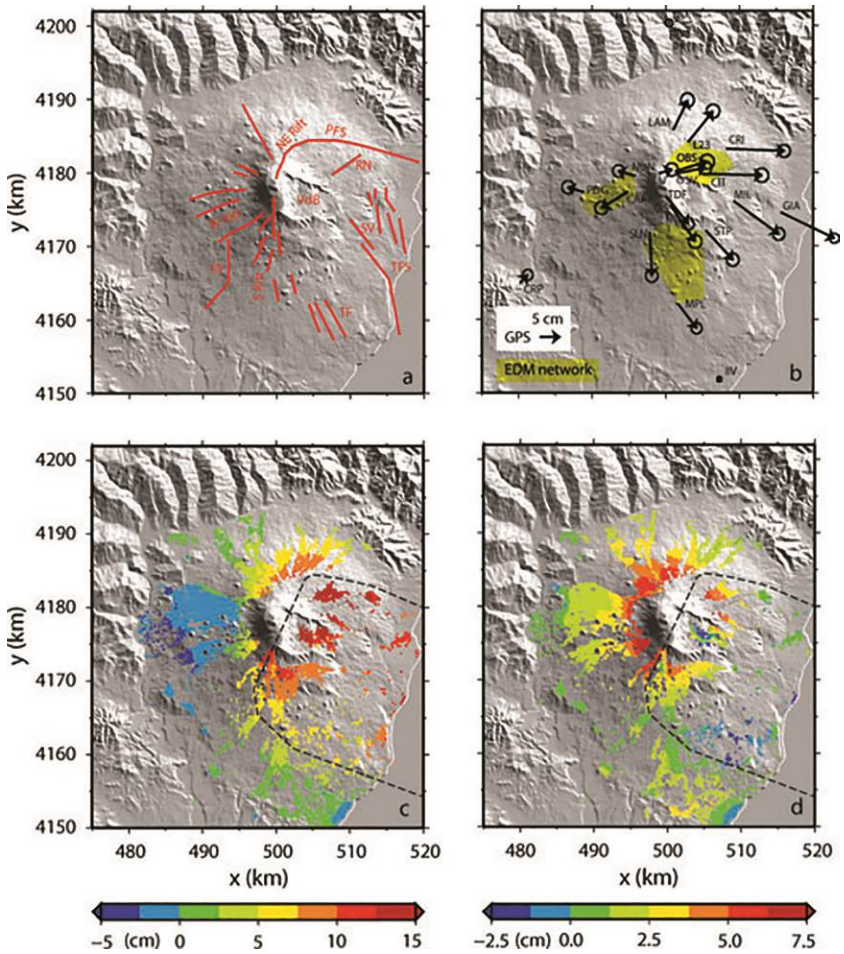

Figure 20: Geodetic data collected between 1993 and 1997 at Mt Etna. (a) Simplified structural map of Mt Etna. VdB: Valle del Bove; PFS: Pernicana Fault System; TFS: Timpe Fault System; RN: Ripe della Naca Faults; SV: Santa Venerina Fault; TF: Trecastagni Fault; RF: Ragalna Fault. Redrawn from Neri et al. (2004). (b) GPS horizontal vectors and associated errors. The translucent yellow areas identify the EDM networks. DInSAR data are shown as a combination of ascending and descending orbits and converted into (c) E–W and (d) vertical displacement components. The dashed line indicates the sector supposed to be subjected to flank instability. From (Trasatti et al., 2009).

5. The way forward

The improved positioning of the satellite, now possibly known with precision of centimeters (Balss et al., 2013) and the good control of the orbit (in the case of Sentinel-1, the orbital radius will be 50 m) make practically irrelevant most of the co-registration, interferogram generation, phase unwrapping, and geocoding problems that affected the early InSAR studies. The azimuthal position of the satellite will be needed to be known to the centimeter to avoid discontinuities in the phases of the focused data, due to the TOPS methodology used (Rodriguez-Cassola et al., 2013). Further, short baselines lead to topography irrelevance, and thus most of the previous problems will be only related to the ever changing atmosphere. Finally, the availability of Numerical Weather Predictions will remove most of the low spatial frequencies of the atmospheric phase screen, leaving only its unpredictable turbulent component (Adam et al., 2013). The future developments of InSAR depend on successful deployment of forthcoming missions. At present, the existing constellations are in X band, with four COSMO-SkyMed satellites staggered in a 16-day orbits to offer 1 to 16-day revisit periods and the two TerraSAR/TanDEM-X spacecrafts, and in C band, including the Canadian RADARSAT-2 and the Indian RISAT-1. New C, X, and L band satellites (Sentinel-1B, the Canadian RADARSAT Constellation Mission, Kompsat5, COSMO-SkyMed-2, ALOS-2 PALSAR, SAOCOM, etc.) have been commissioned in the years after 2013.

To date, most InSAR studies of seismic deformation have been focused on single faults. With the launch of Sentinel-1, high-quality, coherent InSAR data covering all areas of significant seismic hazard will be available in few years. This offers the potential for InSAR data to be combined with GPS to produce regional strain maps (Wang and Wright, 2012). These could significantly increase the spatial resolution and quality of models of global strain (Kreemer et al., 2003) and would be able to provide an independent means for assessing seismic hazard. Similarly, InSAR enables the comprehensive monitoring of nearly all of the more than one thousand active volcanoes on Earth. Clearly there is a need for uninterrupted, complete and optimized InSAR monitoring of most all of the naturally and anthropogenic deformation features.

Sentinel-1A, in its Interferometric Wide Swath (IW) mode is able to systematically acquire InSAR data, operating the C-band 5.7 cm wavelength. It will acquire data for the whole solid Earth surface every 6 when the twin platform Sentinel11B will be made available. The acquisition is over swaths 250 km wide, with systematic intervals, and having a resolution of 5 m (range) x 20 m (azimuth). Both HH and HV polarization data (or VV and VH) will be available, enhancing the sensing capabilities of the system.

The IW is meant for interferometry and is of particular interest for geophysical applications. The impact of the wide swath is significant for tectonic applications in particular, as long wavelength atmospheric artefacts will be under better control. The continuity and regularity of acquisitions will enforce the role of SAR data for the accurate quantification of deformation rates in multi-temporal InSAR techniques.

A lower impact of decorrelation and a better filtering of atmospheric signal will result in a higher spatial density of measurement points (Lanari, 2004). Further, the coherence will be improved thanks also to a tighter orbital control that will maintain the orbital tube within 100 m.

For instance, if the phase component due to water vapour with period 100 km has amplitude of 1 cm, and at least 50% of it can be removed using NWP, a 5 mm peak error is left to be abated in 1 year to less than 1 mm using the 30 available measurements. Therefore, wide area deformation rates of more than 1 mm/year/100km should be made clearly visible in one year.

The availability of very high resolution images will also help for the analysis of local ground motions, for instance, for volcanologic applications. SAR platforms to be available further ahead in time may be such that wider swaths and therefore frequent revisit times will be joined by high resolution.

A reasonable long-term prediction of the technological evolution of SAR imagery is the geosynchronous SAR. Such a system would synthesize the antenna with its relative motion as the geosynchronous orbit would not be perfect, but would involve an apparent elliptical wander of the satellite. Studies are ongoing, and geosynchronous missions are expected in the next 10 years.

In the last years, the scientific community has set out a vision of the EO contribution to the Earth Sciences for the next 5-10 years regarding: i) a high resolution global strain model using InSAR, ii) regional and global maps of active faults, iii) rapid response to earthquakes. In order to achieve such results, the future missions should receive the following topics:

- radar missions should acquire data as often as possible,
- uniform catalogues with single mode of acquisitions for long periods should be available,
- radar missions should acquire in multiple viewing geometries,
- satellite data should have free and open data policies,
- e-infrastructures with unified metadata should allow the management of thousands of radar data.

Additionally, technical requirements concerning the different frequency bands, the spatial resolution, new modeling methods for the analyses of InSAR data, the development of innovative approaches for joint analyses incorporating InSAR and other geophysical data, all these achievements are expected to fulfill the potential of InSAR.

REFERENCES

Adam, N., Rodriguez Gonzalez, F., Parizzi, A., Brcic, R., 2013. Wide area persistent scatterer interferometry: current developments, algorithms and examples, Geoscience and Remote Sensing Symposium (IGARSS), 2013 IEEE International. IEEE, pp. 1857-1860.

Agnesi, V., Camarda, M., Conoscenti, C., Di Maggio, C., Diliberto, I.S., Madonia, P., Rotigliano, E., 2005. A multidisciplinary approach to the evaluation of the mechanism that triggered the Cerda landslide (Sicily, Italy). Geomorphology 65, 101-116.

Agram, P.S., Jolivet, R., Riel, B., Lin, Y.N., Simons, M., Hetland, E., Doin, M.P., Lasserre, C., 2013. New Radar Interferometric Time Series Analysis Toolbox Released. Eos, Transactions American Geophysical Union 94, 69-70.

Albano, M., Barba, S., Saroli, M., Moro, M., Malvarosa, F., Costantini, M., Bignami, C., Stramondo, S., 2015a. Gravity-driven postseismic deformation following the Mw 6.3 2009 L'Aquila (Italy) earthquake. Scientific Reports 5, 16558.

Albano, M., Polcari, M., Bignami, C., Trasatti, E., Moro, M., Stramondo, S., Wegmuller, U., 2015b. Sentinel-1 InSAR: first results from seismic and volcanic applications, EGU General Assembly Conference Abstracts, p. 10109.

Amelung, F., Bell, J.W., 2003. Interferometric synthetic aperture radar observations of the 1994 Double Spring Flat, Nevada, earthquake (M5.9): Main shock accompanied by triggered slip on a conjugate fault. Journal of Geophysical Research-Solid Earth 108, -.

Atzori, S., Hunstad, I., Chini, M., Salvi, S., Tolomei, C., Bignami, C., Stramondo, S., Trasatti, E., Antonioli, A., Boschi, E., 2009. Finite fault inversion of DInSAR coseismic displacement of the 2009 L'Aquila earthquake (central Italy). Geophysical Research Letters 36.

Baer, G., Y., Hamiel, G., Shamir, R., Nof,, 2008. Evolution of a magma-driven earthquake swarm and triggering of the nearby Oldoinyo Lengai eruption, as resolved by InSAR, ground observations and elastic modeling, East African Rift. Earth and Planetary Science Letters 272, 339–352.

Balss, U., Gisinger, C., Cong, X.Y., Brcic, R., Steigenberger, P., Eineder, M., Pail, R., Hugentobler, U., 2013. High resolution geodetic earth observation with TerraSAR-X: Correction schemes and validation, Geoscience and Remote Sensing Symposium (IGARSS), 2013 IEEE International. IEEE, pp. 4499-4502.

Barbot, S., Hamiel, Y., Fialko, Y., 2008. Space geodetic investigation of the coseismic and postseismic deformation due to the 2003 Mw7.2 Altai earthquake: Implications for the local lithospheric rheology. J. Geophys. Res. 113, B03403, doi:03410.01029/02007JB005063.

Barnhart W. D., M.J.W., Rowena B. Lohman, and Andrew K. Melkonian, 2011. InSAR and Optical Constraints on Fault Slip during the 2010–2011 New Zealand Earthquake Sequence. Seismological Research Letters 82, 815-823.

Beavan, J., Fielding, E.J., Motagh, M., Samsonov, S., Donnelly, N., 2011. Fault location and slip distribution of 22 February 2011 Mw 6.3 Christchurch, New Zealand, earthquake from geodetic data. Seismological Research Letters 82, 789-799.

Beavan, J., Motagh, M., Fielding, E.J., Donnelly, N., Collett, D., 2012. Fault slip models of the 2010-2011 Canterbury, New Zealand, earthquakes from geodetic data, and observations of post-seismic ground deformation. New Zealand Journal of Geology & Geophysics.

Beavan, J., Samsonov, S., Motagh, M., Wallace, L., Ellis, S., Palmer, N., 2010. The Darfield (Canterbury) Earthquake: geodetic observations and preliminary source model. Bulletin New Zealand Society for Earthquake Engineering 43, 228-235.

Behr, J., Bilham, R., Bodin, P., Burford, R.O., Bürgmann, R., 1990. Aseismic Slip on the San-Andreas Fault South of Loma-Prieta. Geophysical Research Letters 17, 1445-1448.

Bekaert, D., Hooper, A., Pathier, E., Yun, S., 2010. InSAR time series analysis of the 2006 slow slip event on the Guerrero Subduction Zone, Mexico, p. 03.

Bell, M., Elliott, J., Parsons, B., 2011. Interseismic strain accumulation across the Manyi fault (Tibet) prior to the 1997 Mw 7.6 earthquake. Geophysical Research Letters 38, L24302.

Berardino, P., Fornaro, G., Lanari, R., Sansosti, E., 2002. A new algorithm for surface deformation monitoring based on small baseline differential SAR interferograms. IEEE Trans. Geosci. Remote Sens. 40, 2375-2383.

Bianco, F., E. Del Pezzo, G. Saccorotti, and G. Ventura, 2004. The role of hydrothermal fluids in triggering the July-August 2000 seismic swarm at Campi Flegrei, Italy: evidence from seismological and mesostructural data. Journal of Volcanology and Geothermal Research 133, 229-246.

Biggs, J., Bürgmann, R., Freymueller, J., Lu, Z., Parsons, B.E., Ryder, I., Schmalzle, G., Wright, T., 2009. The postseismic response to the 2002 M7.9 Denali Fault Earthquake: Constraints from InSAR 2003-2005. Geophys J Int 176.

Biggs, J., Wright, T., Lu, Z., Parsons, B., 2007a. Multi-interferogram method for measuring interseismic deformation: Denali Fault, Alaska. Geophys J Int 170, 1165-1179.

Biggs, J., Wright, T., Lu, Z., Parsons, B., 2007b. Multi-interferogram method for measuring interseismic deformation: Denali Fault, Alaska. Geophys. J. Int. 170, 1165-1179.

Bignami, C., Corradini, S., Merucci, L., De Michele, M., Raucoules, D., De Astis, G., Stramondo, S., Piedra, J., 2014. Multisensor Satellite Monitoring of the 2011 Puyehue-Cordon Caulle Eruption. Selected Topics in Applied Earth Observations and Remote Sensing, IEEE Journal of 7, 2786-2796.

Brocher, T.M., Baltay, A.S., Hardebeck, J.L., Pollitz, F.F., Murray, J.R., Llenos, A.L., Schwartz, D.P., Blair, J.L., Ponti, D.J., Lienkaemper, J.J., 2015. The Mw 6.0 24 August 2014 South Napa Earthquake. Seismological Research Letters 86, 309-326.

Bürgmann, R., and W., Thatcher, 2013. Space geodesy: a revolution in crustal deformation measurements of tectonic processes. Geological Society of America Special Paper 500.

Bürgmann, R., Schmidt, D., Nadeau, R.M., d'Alessio, M., Fielding, E.J., Manaker, D., McEvilly, T.V., Murray, M.H., 2000. Earthquake Potential Along the Northern Hayward Fault, California. Science 289, 1178-1182.

Cakir, Z., Akoglu, A.M., Belabbes, S., Ergintav, S., Meghraoui, M., 2005. Creeping along the Ismetpasa section of the North Anatolian fault (Western Turkey): rate and extent from InSAR. Earth and Planetary Science Letters 238, 225-234.

Cavalie, O., Lasserre, C., Doin, M.P., Peltzer, G., Sun, J., Xu, X., Shen, Z.K., 2008. Measurement of interseismic strain across the Haiyuan fault (Gansu, China), by InSAR. Earth and Planetary Science Letters 275, 246-257.

Chini, M., Albano, M., Saroli, M., Pulvirenti, L., Moro, M., Bignami, C., Falcucci, E., Gori, S., Modoni, G., Pierdicca, N., 2015. Coseismic liquefaction phenomenon analysis by COSMO-SkyMed: 2012 Emilia (Italy) earthquake. International Journal of Applied Earth Observation and Geoinformation 39, 65-78.

Chini, M., Atzori, S., Trasatti, E., Bignami, C., Kyriakopoulos, C., Tolomei, C., Stramondo, S., 2010. The May 12, 2008, (Mw 7.9) Sichuan Earthquake (China): Multiframe ALOS-PALSAR DInSAR Analysis of Coseismic Deformation. IEEE Geoscience and Remote Sensing Letters 7.

Chini, M., Bignami, C., Stramondo, S., Pierdicca, N., 2008. Uplift and subsidence due to the 26 December 2004 Indonesian earthquake detected by SAR data. International Journal of Remote Sensing 29, 3891-3910.

Chini, M., Pierdicca, N., Emery, W.J., 2009. Exploiting SAR and VHR optical images to quantify damage caused by the 2003 Bam earthquake. Geoscience and Remote Sensing, IEEE Transactions on 47, 145-152.

Chini, M., Piscini, A., Cinti, F.R., Amici, S., Nappi, R., DeMartini, P.M., 2013. The 2011 Tohoku (Japan) tsunami inundation and liquefaction investigated through optical, thermal, and SAR data. Geoscience and Remote Sensing Letters, IEEE 10, 347-351.

Chini, M., Pulvirenti, L., Pierdicca, N., 2012. Analysis and interpretation of the COSMO-SkyMed observations of the 2011 Japan tsunami. Geoscience and Remote Sensing Letters, IEEE 9, 467-471.

Crosetto, M., Crippa, B., Biescas, E., 2005. Early detection and in-depth analysis of deformation phenomena by radar interferometry. Engineering Geology 79, 81−91.

D'Agostino N., D., Cheloni, G., Fornaro, R., Giuliani, D., Reale, 2012. Space-time distribution of afterslip following the 2009 L'Aquila earthquake. Journal of Geophysical Research 117.

Dawson, J., P. Cummins, P. Tregoning, and M. Leonard, 2008. Shallow intraplate earthquakes in Western Australia observed by Interferometric Synthetic Aperture Radar. J. Geophys. Res. 113.

De Martino, P., Tammaro, U., Obrizzo, F., 2014. GPS time series at Campi Flegrei caldera (2000-2013). Annals of geophysics 57, S0213.

De Michele, M., Raucoules, D., Lasserre, C., Pathier, E., Klinger, Y., Van der Woerd, J., de Sigoyer, J., Xu, X.W., 2010. The M-w 7.9, 12 May 2008 Sichuan earthquake rupture measured by sub-pixel correlation of ALOS PALSAR amplitude images. Earth Planets and Space 62, 875-879.

De Michele, M., Raucoules, D., Rolandone, F., Briole, P., Salichon, J., Lemoine, A., Aochi, H., 2011. Spatiotemporal evolution of surface creep in the Parkfield region of the San Andreas Fault (1993-2004) from synthetic aperture radar. Earth and Planetary Science Letters.

Diao, F., Walter, T., Motagh, M., Prats-Iraola, P., Wang, R., Samsonov, S., 2015. The 2015 Gorkha earthquake investigated from radar satellites: Slip and stress modeling along the MHT. Frontiers in Earth Science 3, 65.

Dvorak, J.J., Dzurisin, D., 1997. Volcano geodesy: The search for magma reservoirs and the formation of eruptive vents. Reviews of Geophysics 35, 343-384.

Dziak, R.P., William W., Chadwick, Jr., Christopher G., Fox, and Robert W., Embley 2003. Hydrothermal temperature changes at the southern Juan de Fuca Ridge associated with MW 6.2 Blanco Transform earthquake Geology 31, 119-122.

Elliott, J., Biggs, J., Parsons, B., Wright, T., 2008. InSAR slip rate determination on the Altyn Tagh Fault, northern Tibet, in the presence of topographically correlated atmospheric delays. Geophysical Research Letters 35.

Elliott, J.R., E. K., N., P. C., E., J. A., J., S., L., Z., L., M., O., and B., P., 2012. Slip in the 2010-2011 Canterbury earthquakes, New Zealand. J. Geophys. Res. 117.

Feigl, K.L., Gasperi, J., Sigmundsson, F., Rigo, A., 2000. Crustal deformation near Hengill volcano, Iceland 1993–1998: Coupling between magmatic activity and faulting inferred from elastic modeling of satellite radar interferograms. Journal of Geophysical Research: Solid Earth 105, 25655-25670.

Feng, G., Ding, X., Li, Z., Mi, J., Zhang, L., Omura, M., 2012. Calibration of an InSAR-Derived Coseimic Deformation Map Associated With the 2011 Mw-9.0 Tohoku-Oki Earthquake. IEEE Geoscience and Remote Sensing Letters 9.

Feng, G., Hetland, E.A., Ding, X., Li, Z., Zhang, L., 2010. Coseismic fault slip of the 2008 Mw 7.9 Wenchuan earthquake estimated from InSAR and GPS measurements. Geophysical Research Letters 37, L01302, doi:01310.01029/02009gl041213.

Feng, G., Jónsson, S., 2012. Shortcomings of InSAR for studying megathrust earthquakes: The case of the Mw9. 0 Tohoku-Oki earthquake. Geophysical Research Letters 39, L10305.

Ferretti, A., Fumagalli, A., Novali, F., Prati, C., Rocca, F., Rucci, A., 2011. A New Algorithm for Processing Interferometric Data-Stacks: SqueeSAR. Geoscience and Remote Sensing, IEEE Transactions on 49, 3460-3470.

Ferretti, A., Prati, C., Rocca, F., 2000. Nonlinear subsidence rate estimation using permanent scatterers in differential SAR interferometry. Ieee Transactions on Geoscience and Remote Sensing 38, 2202-2212.

Fialko, Y., 2004. Evidence of fluid-filled upper crust from observations of postseismic deformation due to the 1992 Mw 7.3 Landers earthquake. Journal of Geophysical Research.

Fialko, Y., Sandwell, D., Agnew, D., Simons, M., Shearer, P., Minster, B., 2002. Deformation on nearby faults induced by the 1999 Hector Mine earthquake. Science 297, 1858-1862.

Fialko, Y., Sandwell, D., Simons, M., Rosen, P.A., 2005. Three-dimensional deformation caused by the Bam, Iran, earthquake and the origin of shallow slip deficit. Nature 435, 295-299, doi:210.1038/nature03425.

Fielding, E.J., Lundgren, P.R., Bürgmann, R., Funning, G.J., 2009a. Shallow fault-zone dilatancy recovery after the 2003 Bam earthquake in Iran. Nature 458, 64-68.

Fielding, E.J., Lundgren, P.R., Bürgmann, R., Funning, G.J., 2009b. Shallow fault-zone dilatancy recovery after the 2003 Bam earthquake in Iran. Nature 458, 64-68.

Fielding, E.J., Sladen, A., Li, Z., Avouac, J.-P., Bürgmann, R., Ryder, I., 2013. Kinematic fault slip evolution source models of the 2008 M7.9 Wenchuan earthquake in China from SAR interferometry, GPS and teleseismic analysis and implications for Longmen Shan tectonics. Geophys J Int 194, 1138-1166.

Fielding, E.J., Wright, T.J., Muller, J., Parsons, B.E., Walker, R., 2004. Aseismic deformation of a fold-and-thrust belt imaged by synthetic aperture radar interferometry near Shahdad, southeast Iran. Geology 32, 577-580.

Foumelis, M., Trasatti, E., Papageorgiou, E., Stramondo, S., Parcharidis, I., 2013. Monitoring Santorini volcano (Greece) breathing from space. Geophys J Int 193, 161-170.

Fukushima, Y., Y., T., and M., H., 2013. Complex ruptures of the 11 April 2011 Mw 6.6 Iwaki earthquake triggered by the 11 March 2011 Mw 9.0 Tohoku earthquake, Japan. Bull. Seismol. Soc. Am. 103, 1572–1583.

Funning, G.J., Bürgmann, R., Ferretti, A., Novali, F., Fumagalli, A., 2007. Creep on the Rodgers Creek fault, northern San Francisco Bay area from a 10 year PS-InSAR dataset. Geophysical Research Letters 34.

Funning, G.J., Parsons, B.E., Wright, T.J., Jackson, J.A., Fielding, E.J., 2005. Surface displacements and source parameters of the 2003 Bam (Iran) earthquake from Envisat advanced synthetic aperture radar imagery. J. Geophys. Res. 110, B09406,doi:09410.01029/02004JB003338.

Furuya, M., Kobayashi, T., Takada, Y., Murakami, M., 2010. Fault Source Modeling of the 2008 Wenchuan Earthquake Based on ALOS/PALSAR Data. Bulletin of the Seismological Society of America 100, 2750-2766.

Furuya, M., Satyabala, S.P., 2008. Slow earthquake in Afghanistan detected by InSAR. Geophys. Res. Lett 35, L06309.

Gabriel, A.K., Goldstein, R.M., Zebker, H.A., 1989. Mapping small elevation changes over large areas—differential radar interferometry. Journal of Geophysical Research 94, 9183–9191.

Goldstein, R.M., Engelhardt, H., Kamb, B., Frolich, R.M., 1993. Satellite radar interferometry for monitoring ice sheet motion—application to an Antarctic ice stream. Science 262, 1525–1530.

Guglielmino, F., Bignami, C., Bonforte, A., Briole, P., Obrizzo, F., Puglisi, G., Stramondo, S., Wegmüller, U., 2011. Analysis of satellite and in situ ground deformation data integrated by the SISTEM approach: The April 3, 2010 earthquake along the Pernicana fault (Mt. Etna - Italy) case study. Earth and Planetary Science Letters 312, 327-336

Hao, K.X., Si, H.J., Fujiwara, H., Ozawa, T., 2009. Coseismic surface-ruptures and crustal deformations of the 2008 Wenchuan earthquake Mw7.9, China. Geophysical Research Letters 36, L11303, doi: 11310.11029/12009gl037971.

He, P., Y., W., C., X., and Y., L., 2013. The large aftershocks triggered by the 2011 Mw 9.0 Tohoku-Oki earthquake, Japan. Journal of Asian Earth Sciences 74, 1-10.

Hetland, E.A., Musé, P., Simons, M., Lin, Y.N., Agram, P.S., DiCaprio, C.J., 2012. Multiscale InSAR Time Series (MInTS) analysis of surface deformation. Journal of Geophysical Research: Solid Earth 117, B02404.

Hill, D.P., 1977. A model for earthquake swarms. J. Geophys. Res. 82, 1347–1352.

Hooper, A., 2008. A multi-temporal InSAR method incorporating both persistent scatterer and small baseline approaches. Geophysical Research Letters 35.

Hooper, A., Bekaert, D., Spaans, K., Arıkan, M., 2011. Recent advances in SAR interferometry time series analysis for measuring crustal deformation. Tectonophysics.

Hooper, A., Zebker, H., Segall, P., Kampes, B., 2004. A new method for measuring deformation on volcanoes and other natural terrains using InSAR persistent scatterers. Geophysical Research Letters 31.

Hsu, L., Bürgmann, R., 2006. Surface creep along the Longitudinal Valley fault, Taiwan from InSAR measurements. Geophys. Res. Lett 33.

Jacobs, A., Sandwell, D., Fialko, Y., Sichoix, L., 2002. The 1999 (Mw 7.1) Hector Mine, California, earthquake: Near-field postseismic deformation from ERS interferometry. Bulletin of the Seismological Society of America 92, 1433-1442.

Johanson, I., Bürgmann, R., 2005. Creep and quakes on the northern transition zone of the San Andreas fault from GPS and InSAR data. Geophys. Res. Lett 32, L14.

Johanson, I., Fielding, E., Rolandone, F., Burgmann, R., 2006. Coseismic and postseismic slip of the 2004 Parkfield earthquake from space-geodetic data. Bulletin of the Seismological Society of America 96, S269-S282.

Jolivet, R., Cattin, R., Chamotrooke, N., Lasserre, C., Peltzer, G., 2008. Thin-plate modeling of interseismic deformation and asymmetry across the Altyn Tagh fault zone. Geophysical Research Letters 35.

Jónsson, S., Segall, P., Pedersen, R., Bjornsson, G., 2003. Post-earthquake ground movements correlated to pore-pressure transients. Nature 424, 179-183.

Keefer, D.K., 1984. Landslides caused by earthquakes. Geological Society of America Bulletin 95, 406-421.

Keefer, D.K., 2002. Investigating landslides caused by earthquakes–a historical review. Surveys in Geophysics 23, 473-510.

Kozaci, O., Dolan, J., Finkel, R., Hartleb, R., 2007. Late Holocene slip rate for the North Anatolian fault, Turkey, from cosmogenic 36Cl geochronology: Implications for the constancy of fault loading and strain release rates. Geology 35, 867.

Kreemer, C., Holt, W.E., Haines, A.J., 2003. An integrated global model of present-day plate motions and plate boundary deformation. Geophys J Int 154, 8-34.

Kyriakopoulos C., M.C., C. Bignami, S. Stramondo, A. Ganas, M. Kolligri, A. Moshou, 2013. Monthly migration of a tectonic seismic swarm detected by DInSAR: Southwest Peloponnese, Greece. Geophys. J. Int.

Lacroix, P., Perfettini, H., Taipe, E., Guillier, B., 2014. Coseismic and postseismic motion of a landslide: Observations, modeling, and analogy with tectonic faults. Geophysical Research Letters 41, 6676-6680.

Lanari, R., Mora, O., Manunta, M., Mallorqui, J.J., Berardino, P., Sansosti, E., 2004. A small-baseline approach for investigating deformations on full-resolution differential SAR interferograms. IEEE Trans. Geosci. Remote Sens. 42, 1377-1386.

Lanari, R., Mora, O., Manunta, M., Mallorqui, J., Berardino, P., & Sansosti, E. , 2004. A Small Baseline Approach for Investigating Deformations on Full Resolution Differential SAR Interferograms. IEEE Trans. Geosci. Remote Sensing 42, 1377-1386.

Lohman, R., McGuire, J., 2007. Earthquake swarms driven by aseismic creep in the Salton Trough, California. J. geophys. Res 112, B04405.

Lu, Z., J. Power, V. McConnell, C. Wicks, and D. Dzurisin, 2002. Pre-Eruptive Inflation and Surface Interferometric Coherence Characteristics Revealed by Satellite Radar Interferometry at Makushin Volcano, Alaska: 1993 - 2000. Journal of Geophysical Research 107.

Lu, Z., T. Masterlark, D. Dzurisin, R. Rykhus, and C. Wicks, 2003. Magma Supply Dynamics at Westdahl Volcano, Alaska, Modeled from Satellite Radar Interferometry. Journal of Geophysical Research 108.

Marone, C.J., C. H., Scholz, and, R. G., Bilham 1991. On the mechanics of earthquake afterslip. Journal of Geophysical Research 96, 8441-8452.

Massonnet, D., Feigl, K., Rossi, M., Adragna, F., 1994. Radar interferometric mapping of deformation in the year after the Landers earthquake. Nature 369, 227–230.

Massonnet, D., Feigl, K.L., 1998. Radar interferometry and its application to changes in the Earth's surface. Reviews of geophysics 36, 441-500.

Massonnet, D., Rossi, M., Carmona, C., Adragna, F., Peltzer, G., Feigl, K., Rabaute, T., 1993. The displacement field of the Landers earthquake mapped by radar interferometry. Nature 364, 138–142.

Massonnet, D., Thatcher, W., Vadon, H., 1996. Detection of postseismic fault-zone collapse following the Landers earthquake. Nature 382, 612–616.

Mogi, K., 1963. Some discussions on aftershocks, foreshocks, and earthquake swarms. Bull. Earthq. Res. Inst. Univ. Tokyo 41, 615–658.

Mora, O., Mallorquí, J.J., Broquetas, A., 2003. Linear and nonlinear terrain deformation maps from a reduced set of interferometric SAR images. IEEE Trans. Geosci. Remote Sensing 41, 2243−2253.

Moro, M., Chini, M., Saroli, M., Atzori, S., Stramondo, S., Salvi, S., 2011. Analysis of large, seismically induced, gravitational deformations imaged by high-resolution COSMO-SkyMed synthetic aperture radar. Geology 39, 527-530.

Moro, M., Saroli, M., Salvi, S., Stramondo, S., Doumaz, F., 2007. The relationship between seismic deformation and deep-seated gravitational movements during the 1997 Umbria–Marche (Central Italy) earthquakes. Geomorphology 89, 297-307.

Motagh, M., Beavan, J., Fielding, E.J., Haghshenas, M., 2014. Postseismic ground deformation following the september 2010 darfield, New Zealand, earthquake from TerraSAR-X, COSMO-SkyMed, and ALOS InSAR. Geoscience and Remote Sensing Letters, IEEE 11, 186-190.

Mrlina, J., and M., Seidl,, 2008. Relation of surface movements in West Bohemia to earthquake swarms. Studia Geophysica et Geodaetica 52, 549-566.

Murakami, M., M. Tobita, S. Fujiwara, T. Saito, and H. Masaharu 1996. Coseismic crustal deformations of 1994 Northridge, California, earthquake detected by interferometric JERS 1 synthetic aperture radar. J. Geophys. Res. 101, 8605–8614.

Neri, M., Casu, F., Acocella, V., Solaro, G., Pepe, S., Berardino, P., Sansosti, E., Caltabiano, T., Lundgren, P., Lanari, R., 2009. Deformation and eruptions at Mt. Etna (Italy): A lesson from 15 years of observations. Geophysical Research Letters 36.

Ozawa, S., Murakami, M., Fujiwara, S., Tobita, M., 1997. Synthetic aperture radar interferogram of the 1995 Kobe earthquake and its geodetic inversion. Geophysical Research Letters 24, 2327-2330.

Pallister, J.S., Wendy A. McCausland,Sigurjón Jónsson,Zhong Lu, Hani M. Zahran, Salah El Hadidy,Abdallah Aburukbah, Ian C. F. Stewart,Paul R. Lundgren,Randal A. White & Mohammed R. H. Moufti,, 2010. Broad accommodation of rift-related extension recorded by dyke intrusion in Saudi Arabia. Nature Geoscience 3, 705–712

Peltzer, G., Hudnut, K.W., Feigl, K.L., 1994. Analysis of coseismic surface displacement gradients using radar interferometry - new insights into the Landers earthquake. Journal Of Geophysical Research 99, 21971-21981.

Peltzer, G., Rosen, P., Rogez, F., Hudnut, K., 1996. Postseismic rebound in fault step-overs caused by pore fluid-flow. Science 273, 1202–1204.

Peltzer, G., Rosen, P., Rogez, F., Hudnut, K., 1998. Poroelastic rebound along the Landers 1992 earthquake surface rupture. J. Geophys. Res. 103, 30131-30145.

Pollard, D.D., Delaney, P.T., Duffield, W.A., Endo, E.T., Okamura, A.T., 1983. Surface deformation in volcanic rift zones. Tectonophysics 94, 541-584.

Pollitz, F.F., Peltzer, G., Bürgmann, R., 2002. Mobility of continental mantle: Evidence from postseismic geodetic observations following the 1992 Landers earthquake. Journal of Geophysical Research 418, 167-171.

Pollitz, F.F., Wicks, C., Thatcher, W., 2001. Mantle flow beneath a continental strike-slip fault: Postseismic deformation after the 1999 Hector Mine earthquake. Science 293, 1814-1818.

Pritchard, M.E., C. Ji, and M. Simons, 2006. Distribution of slip from 11 MW > 6 earthquakes in the northern Chile subduction zone. J. Geophys. Res.

Pritchard, M.E., Jay, J.A., Aron, F., Henderson, S.T., and Lara, L.E., 2013. Subsidence at southern Andes volcanoes induced by the 2010 Maule, Chile earthquake. Nature Geoscience.

Reale, D., Nitti, D.O., Peduto, D., Nutricato, R., Bovenga, F., Fornaro, G., 2011. Postseismic Deformation Monitoring With the COSMO/SKYMED Constellation. IEEE Geoscience and Remote Sensing Letters 8, 696 – 700.

Reid, H.F., 1910. Permanent displacements of the ground, in the California earthquake of April 18, 1906. Report of the State Earthquake Investigation Commission, 16-28.

Rodriguez-Cassola, M., Prats-Iraola, P., De Zan, F., Scheiber, R., Reigber, A., 2013. Doppler-related focusing aspects in the TOPS imaging mode, Geoscience and Remote Sensing Symposium (IGARSS), 2013 IEEE International. IEEE, pp. 2043-2046.

Rogers, G., Dragert, H., 2003. Episodic Tremor and Slip on the Cascadia Subduction Zone: The Chatter of Silent Slip. Science 300, 1942-1943.

Roland, E., McGuire, J.J., 2009. Earthquake swarms on transform faults. Geophys. J. Int. 178, 1677–1690.

Rosen, P.A., Werner, C., Fielding, E.J., Hensley, S., Buckley, S., Vincent, P., 1998. Aseismic creep along the San Andreas Fault at Parkfield, California, measured by radar interferometry. Geophysical Research Letters 25, 825–828.

Rosi, M., Principe, C., Vecci, R., 1993. The 1631 Vesuvius eruption. A reconstruction based on historical and stratigraphical data. Journal of Volcanology and Geothermal Research 58, 151-182.

Rubin, A.M., Pollard, D.D., 1988. Dike-induced faulting in rift zones of Iceland and Afar. Geology 16, 413-417.

Ryder, I., Parsons, B., Wright, T.J., Funning, G.J., 2007. Post-seismic motion following the 1997 Manyi (Tibet) earthquake: InSAR observations and modelling. Geophys J Int 169, 1009-1027.

Rymer, M.J., Treiman, J.A., Kendrick, K.J., Lienkaemper, J.J., Weldon, R.J., Bilham, R., Wei, M., Fielding, E.J., Hernandez, J.L., Olson, B.P.E., Irvine, P.J., Knepprath, N., Sickler, R.R., Tong, X., Siem, M.E., 2011. Triggered surface slips in southern California associated with the 2010 El Mayor-Cucapah, Baja California, Mexico, earthquake, Open-File Report 2010–1333. U.S. Geological Survey, p. 62.

Sandwell, D.T., Sichoix, L., Smith, B., 2002. The 1999 Hector Mine Earthquake, Southern California: Vector Near-Field Displacements from ERS InSAR. BULLETIN OF THE SEISMOLOGICAL SOCIETY OF AMERICA 92, 1341-1354.

Sang-Hoon, H., and Shimon, Wdowinski,, 2011. Evaluation of the quad-polarimetric Radarsat-2 observations for the wetland InSAR application. Can. J. Remote Sensing 37, 1-9.

Schmidt, D.A., and, Bürgmann, R., 2003. Time dependent land uplift and subsidence in the Santa Clara valley, California, from a large InSAR data set. Journal of Geophysical Research 108.

Schmidt, D.A., R., B., R. M., N., M. A., d.A., 2005. Distribution of aseismic slip-rate on the Hayward fault inferred from seismic and geodetic data. Journal of Geophysical Research 110.

Schmidt, D.A., R. Bürgmann, R. M. Nadeau, and M. A. d'Alessio, 2005. Distribution of aseismic slip-rate on the Hayward fault inferred from seismic and geodetic data. Journal of Geophysical Research 110.

Shen, Z.K., Sun, J.B., Zhang, P.Z., Wan, Y.G., Wang, M., Burgmann, R., Zeng, Y.H., Gan, W.J., Liao, H., Wang, Q.L., 2009. Slip maxima at fault junctions and rupturing of barriers during the 2008 Wenchuan earthquake. Nature Geoscience 2, 718-724.

Shirzaei, M., 2012. A wavelet based multitemporal DInSAR algorithm for monitoring ground surface motion. Geoscience and Remote Sensing Letters.

Shirzaei, M., and R. Bürgmann 2013. Time-dependent model of creep on the Hayward fault from joint inversion of 18 years of InSAR and surface creep data. J .Geophys. Res.

Simons, M., Fialko, Y., Rivera, L., 2002. Coseismic deformation from the 1999 Mw 7.1 Hector Mine, California, earthquake as inferred from InSAR and GPS observations. Bulletin of the Seismological Society of America 92, 1390-1402.

Stramondo, S., Bignami, C., Chini, M., Pierdicca, N., Tertulliani, A., 2006. Satellite radar and optical remote sensing for earthquake damage detection: results from different case studies. International Journal of Remote Sensing 27, 4433-4447.

Stramondo, S., Chini, M., Bignami, C., Salvi, S., Atzori, S., 2011a. X-, C-, and L-Band DInSAR Investigation of the April 6, 2009, Abruzzi Earthquake. IEEE Geoscience and Remote Sensing Letters 8, 49-53.

Stramondo, S., Chini, M., Bignami, C., Salvi, S., Atzori, S., 2011b. X-, C-, and L-Band DInSAR Investigation of the April 6, 2009, Abruzzi Earthquake. IEEE Geoscience and Remote Sensing Letters 8, 49-53

Stramondo, S., Kyriakopoulos, C., Bignami, C., Chini, M., Melini, D., Moro, M., Picchiani, M., Saroli, M., Boschi, E., 2011c. Did the September 2010 (Darfield) earthquake trigger the February 2011 (Christchurch) event? Scientific Reports 1.

Stramondo, S., Moro, M., Tolomei, C., Cinti, F.R., Doumaz, F., 2005. InSAR surface displacement field and fault modelling for the 2003 Bam earthquake (southeastern Iran). Journal of Geodynamics.

Sugawara, D., Matsumoto, F., Koji, M., 2012. The 2011 Tohoku-oki Earthquake Tsunami: Similarities and Differences to the 869 Jogan Tsunami on the Sendai Plain. Pure and Applied Geophysics.

Sykes, L.R., 1970. Earthquake swarms and sea-floor spreading. J. Geophys. Res. 75, 6598–6611.

Talebian, M., Fielding, E.J., Funning, G.J., Jackson, J.A., Nazari, H., Parsons, B.E., Priestley, K., Ghorashi, M., Rosen, P.A., Walker, R., Wright, T.J., 2004. The 2003 Bam (Iran) earthquake: rupture of a blind fault. Geophys. Res. Lett 31, L11611, doi:11610.11029/12004GL020058.

Tapponnier, P., Xu, Z.Q., Roger, F., Meyer, B., Arnaud, N., Wittlinger, G., Yang, J.S., 2001. Geology - Oblique stepwise rise and growth of the Tibet plateau. Science 294, 1671-1677.

Taylor, M., Peltzer, G., 2006. Current slip rates on conjugate strike-slip faults in central Tibet using synthetic aperture radar interferometry. Journal of Geophysical Research-Solid Earth 111.

Tobita, M., Fujiwara, S., Ozawa, S., Rosen, P.A., Fielding, E.J., Werner, C.L., Murakami, M., Nakagawa, H., Nitta, K., Murakami, M., 1998. Deformation of the 1995 North Sakhalin earthquake detected by JERS-1/SAR interferometry. Earth Planets Space 50, 313–325.

Tomokazu Kobayashi, Y.T., Masato Furuya, and Makoto Murakami, 2009. Locations and types of ruptures involved in the 2008 Sichuan earthquake inferred from SAR image matching. GEOPHYSICAL RESEARCH LETTERS 36.

Tong, X., Sandwell, D.T., Fialko, Y., 2010. Coseismic slip model of the 2008 Wenchuan earthquake derived from joint inversion of interferometric synthetic aperture radar, GPS, and field data. J. Geophys. Res. 115, B04314.

Trasatti, E., Cianetti, S., Giunchi, C., Bonafede, M., Agostinetti, N.P., Casu, F., Manzo, M., 2009. Bayesian source inference of the 1993-1997 deformation at Mount Etna (Italy) by numerical solutions. Geophys J Int 177, 806-814.

Trasatti, E., Polcari, M., Bonafede, M., Stramondo, S., 2015. Geodetic constraints to the source mechanism of the 2011–2013 unrest at Campi Flegrei (Italy) caldera. Geophysical Research Letters 42, 3847-3854.

Usai, S., 2003. A least squares database approach for SAR interferometric data. Geoscience and Remote Sensing, IEEE Transactions on 41, 753-760.

Vidale, J.E., and P. M., Shearer, , 2006. A survey of 71 earthquake bursts across southern California: Exploring the role of pore fluid pressure fluctuations and aseismic slip as drivers. J. Geophys. Res. 111.

Wang, H., Wright, T., 2012. Satellite geodetic imaging reveals high strain away from major faults of Western Tibet. Geophys. Res. Lett. Minor Corrections.

Wang, H., Wright, T., Biggs, J., 2009. Interseismic slip rate of the northwestern Xianshuihe fault from InSAR data. Geophysical Research Letters 36.

Wei, M., Sandwell, D., Fialko, Y., Bilham, R., 2011. Slip on faults in the Imperial Valley triggered by the 4 April 2010 Mw 7.2 El Mayor-Cucapah earthquake revealed by InSAR. Geophysical Research Letters 38, L01308.

Wei, M., Sandwell, D, Fialko, Y,, 2009. A silent M-w 4.7 slip event of October 2006 on the Superstition Hills fault, southern California. Journal of Geophysical Research-Solid Earth 114.

Werner, C., Wegmuller, U., Strozzi, T., Wiesmann, A., 2003. Interferometric point target analysis for deformation mapping. Proceedings of IGARSS '03 7, 4362−4364.

Weston, J., Ana, M., G. Ferreira, G. J., F., 2012. Systematic comparisons of earthquake source models determined using InSAR and seismic data. Tectonophysics, 532-535.

Weston, J., Ferreira, A., Funning, G., 2011. Global compilation of interferometric synthetic aperture radar earthquake source models: 1. Comparisons with seismic catalogs. J. geophys. Res 116.

Wicks, C., C., Weaver, P., Bodin, and B., Sherrod,, 2013. InSAR Evidence for an active shallow thrust fault beneath the city of Spokane Washington, USA. J. Geophys. Res. Solid Earth 118.

Wicks, C., W., T., C., W., J., G., A., R., P., B., 2011. InSAR observations of aseismic slip associated with an earthquake swarm in the Columbia River flood basalts. J. Geophys. Res. 116.

Wright, T., Parsons, B., England, P., Fielding, E., 2004. InSAR observations of low slip rates on the major faults of western Tibet. Science 305, 236-239.

Wright, T.J., Elliott, J.R., Wang, H., Ryder, I., 2013. Earthquake cycle deformation and the Moho: Implications for the rheology of continental lithosphere. Tectonophysics.

Wright, T.J., Fielding, E.J., Parsons, B.E., 2001. Triggered slip: observations of the 17 August 1999 Izmit (Turkey) earthquake using radar interferometry. Geophysical Research Letters 28, 1079-1082, doi:1010.1029/2000GL011776.

Zebker, H.A., Rosen, P., 1994. On the derivation of coseismic displacement fields using differential radar interferometry: The Landers earthquake, Geoscience and Remote Sensing Symposium, 1994. IGARSS'94. Surface and Atmospheric Remote Sensing: Technologies, Data Analysis and Interpretation., International. IEEE, pp. 286-288.